Chapter 6

Synthesis, Characterization, and Antimicrobial Properties of Indole-Tethered Benzothiazole and Triazole Hybrids

6.1 Introduction

The broad range of pharmacological properties exhibited by indole, benzothiazole, and 1,2,3-triazole scaffolds has attracted significant attention. The versatile biological activities exhibited by indole derivatives, including their anticancer, antioxidant, and antimicrobial properties, have established their indispensability in novel therapeutic agent development.[274] Benzothiazole derivatives, on the other hand, have been extensively studied for their antimicrobial and antifungal activities.[275] The 1,2,3-triazole ring system, introduced via the widely utilized copper(I)-catalyzed azide-alkyne cycloaddition (CuAAC) "click" chemistry, is renowned for its stability and ability to form strong hydrogen bonds, making it a valuable pharmacophore in drug development.[276] Triazole-containing compounds have demonstrated significant biological activities, including antimicrobial, antidiabetic, anticancer, and antiviral properties.[277]

In light of these considerations, our research focused on the synthesis of novel indole-based benzothiazole and 1,2,3-triazole hybrids, aiming to exploit the synergistic effects of these heterocyclic systems. The synthesized compounds were meticulously characterized using ^{1}H NMR, mass spectrometry, and IR spectroscopy, ensuring the structural authenticity and purity of the compounds. Biological evaluations were conducted to assess their antifungal activity against a panel of microbial and fungal strains, with a particular focus on Candida albicans, a common fungal pathogen responsible for severe infections in immunocompromised patients. The results of these assays revealed that several compounds exhibited potent and selective inhibition of Candida albicans, surpassing the antifungal activity of currently available treatments, such as griseofulvin.

To further elucidate the mode of action of these compounds, molecular docking studies were performed against ergosterol, the primary sterol in the fungal cell membrane of Candida albicans. The docking results indicated that the synthesized compounds form

strong binding interactions with ergosterol, suggesting a mechanism of action similar to that of known triazole antifungals, but with enhanced efficacy. These interactions were characterized by hydrogen bonding and hydrophobic interactions that contribute to the stability of the compound-ergosterol complex. Such interactions not only disrupt the integrity of the fungal cell membrane but also prevent the proper function of membrane-bound proteins, leading to fungal cell death.

The compelling antifungal activities observed in this study highlight the potential of indole-based benzothiazole and 1,2,3-triazole hybrids as novel antifungal agents. By integrating the distinct pharmacophoric features of these three heterocycles, we have designed compounds with enhanced biological activity and specificity against Candida albicans. This study not only adds to the growing body of knowledge on the therapeutic potential of heterocyclic compounds but also provides a solid foundation for the development of new antifungal therapies aimed at overcoming the limitations of current treatments.

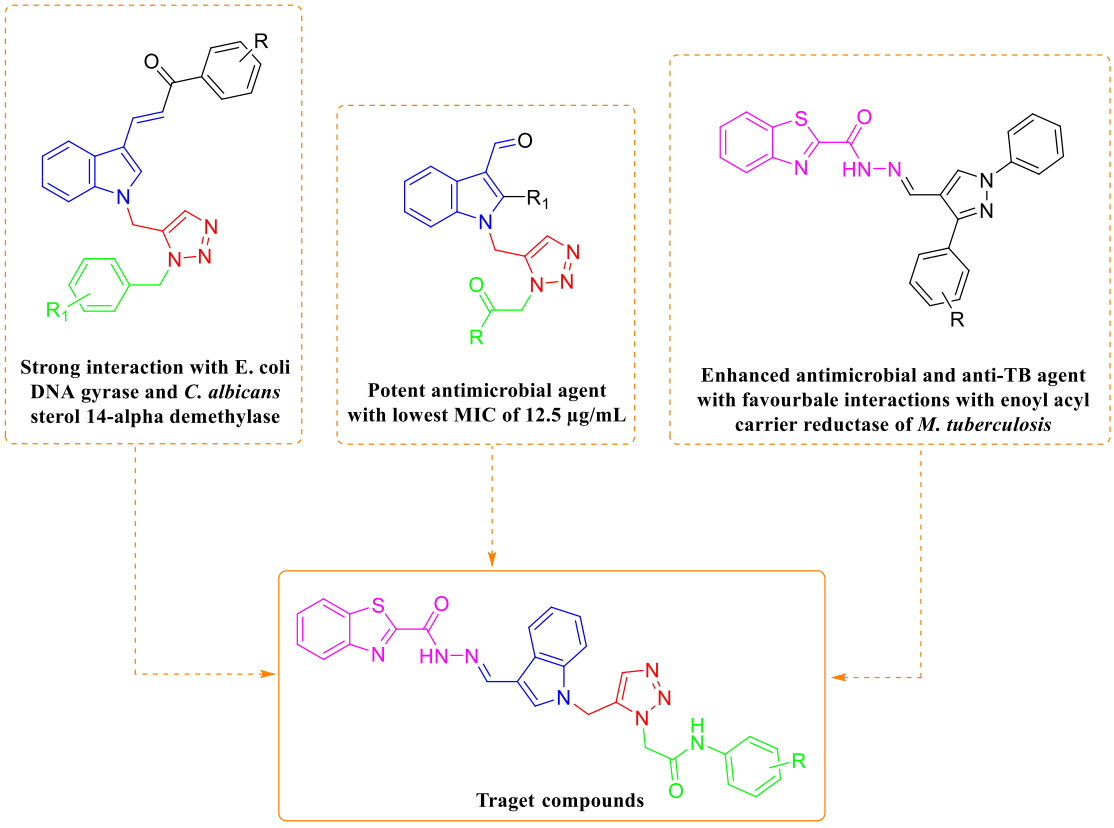

Figure 1: Design of the compounds

6.2 Results and discussion

6.2.1 Chemistry

A multi-step synthetic approach was employed to achieve the synthesis of indole-based benzothiazole and 1,2,3-triazole derivatives. This approach was meticulously designed to incorporate pharmacologically relevant moieties into a unified molecular structure. The nucleophilic substitution reaction of indole-3-carbaldehyde **1** with propargyl bromide, using K_2CO_3 as a base in DMF at ambient temperature, led to the formation of intermediate **2**. This intermediate served as a versatile precursor for the subsequent copper-catalyzed azide-alkyne cycloaddition (CuAAC) reaction. The azide derivatives **5a-j** were synthesized starting from aniline derivatives **3a-j**. The aniline derivatives underwent acylation using chloroacetyl chloride and K_2CO_3 in acetone at room temperature, producing 2-chloro-N-phenylacetamide derivatives **4a-j**. Subsequently, these intermediates were converted to the corresponding azide derivatives **5a-j** through a reaction with NaN_3 in DMF at room temperature, demonstrating a straightforward and efficient route to access the desired azide substrates. The 1,2,3-triazole derivatives **6a-j** were obtained by reacting intermediate **2** with various azides **5a-j** in the presence of catalytic amounts of copper catalyst and sodium ascorbate in DMF. The intermediate triazoles **6a-j** reacted with benzothiazole hydrazide **7** using acetic acid and methanol under reflux conditions. This step effectively yielded the final indole-benzothiazole-triazole hybrids **8a-j**, ensuring the high yield and purity of the products.

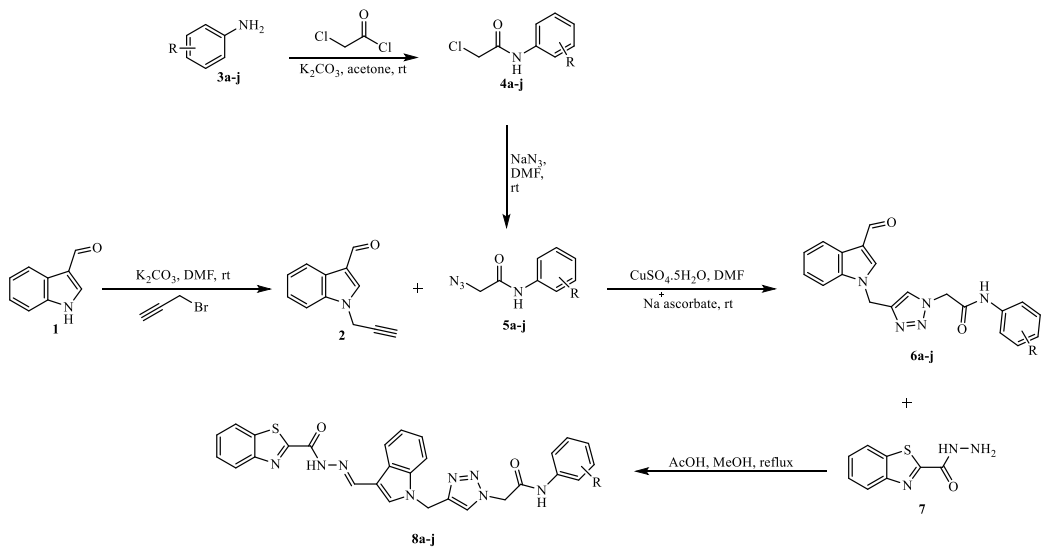

Scheme 1: Synthesis route of indole-based benzothiazole and 1,2,3-triazole derivatives 8a-j via propargylation, Cu-catalyzed azide-alkyne cycloaddition, and condensation reactions

The structural elucidation of derivative **8f** was confirmed through a comprehensive analysis of ^{1}H NMR, ^{13}C NMR DEPT-135, FT-IR, and mass spectrometry, each technique providing complementary evidence of the compound's integrity. The ^{1}H NMR spectrum exhibited significant signals, including the NH proton of the hydrazide moiety appearing as a singlet at δ 12.45 ppm, which was supported by an NH stretching vibration observed in the IR spectrum at 3279.10 cm^{-1}. The singlet at δ 8.86 ppm, corresponding to the imine proton (CH=N) of the indole unit, was further validated by the DEPT-135 spectrum, which displayed a corresponding imine carbon signal at δ 147.33 ppm, confirming the imine functionality. Aromatic protons were observed in the ^{1}H NMR spectrum within the range of δ 7.25-8.34 ppm, indicative of indole, phenyl acetamide and benzothiazole aromatic systems. This aromatic character was also supported by multiple carbon signals in the DEPT-135 spectrum between δ 111.28 and 129.29 ppm, corresponding to aromatic carbons, and was consistent with the IR absorption bands observed between 1400 and 1600 cm^{-1}, which are characteristic of aromatic C=C stretching vibrations. The methylene protons, appearing as singlets at δ 5.60 and 5.34 ppm in the ^{1}H NMR spectrum, aligned with the ^{13}C NMR DEPT-135 signals at δ 52.71 ppm and δ 41.56 ppm, confirming -CH_2- groups that connect the triazole with indole and acetamide moieties. Further structural validation came from mass spectrometry, where the molecular ion peak at m/z 571.1 $(M + H)^{+}$ confirmed the calculated molecular weight of **8f**, corresponding to the formula $C_{28}H_{21}ClN_8O_2S$. The successful synthesis of compounds was definitively confirmed by the consistent data from ^{1}H and ^{13}C NMR and FT-IR spectra. This confirms the indole, benzothiazole, and 1,2,3-triazole frameworks within the single molecule.

6.2.2 *In vitro* antimicrobial evaluation and structural activity relationship studies

In vitro antimicrobial activity against pathogenic bacterial and fungal strains was evaluated for synthesized indole-benzothiazole-1,2,3-triazole derivatives **8a-j**. The antibacterial activity was tested against *Ac. baumannii*, *P. aeruginosa*, *S. aureus*, and *S. pyogenes*, while the antifungal activity was assessed against *C. albicans*, *A. niger*, and *A. clavatus*, using minimal inhibitory concentration (MIC) values **(supplementary Table S1)** to quantify the

efficacy. The heatmap in **Figure 2** demonstrates the MIC values of each compound against different strains, facilitating a comprehensive comparison of their antimicrobial effectiveness. The synthesized compounds **8a-j** were evaluated for further MIC50, MIC90, Geometric mean MIC, MIC ranges, and fold differences, as shown in **Table 1**.

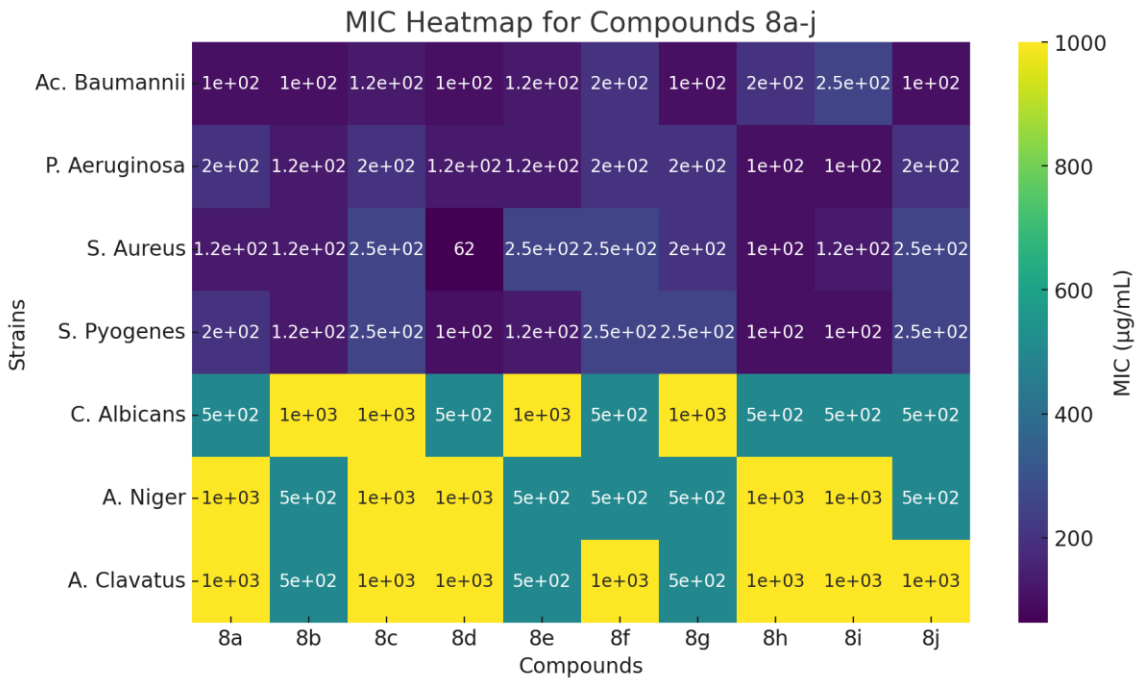

Figure 2: Heatmap of MIC Values for Compounds 8a-j Against Bacterial and Fungal Strains. The color gradient represents the range of MIC values, with darker shades indicating lower MICs and higher antimicrobial potency

The compound **8d** exhibited notable characteristics among the tested compounds, including a low MIC value of 62.5 µg/mL against *S. aureus* and significant potency against *A. baumannii*. The antibacterial activity of **8d** is likely enhanced by ortho-dimethyl groups, which improve lipophilicity and membrane penetration. The compounds **8a** (2,4-xylidine) and **8i** (4-CH_3) also showed strong antibacterial activity, indicating that the addition of methyl groups improves their interaction with bacterial strains. Derivatives containing halogen substitutions, such as **8f**, **8g**, and **8h**, showed moderate activity. The meta positioned chlorine in **8h** exhibited strong activity against bacterial and fungal strains, particularly *P. aeruginosa* and *C. albicans*. Compounds with halogen substituents had varied efficacy, suggesting that the effects of halogens on activity are influenced by electronic and steric factors. Compounds **8c** (2,6-difluoro) and **8e** (4-F) showed selective

activity, with 8e demonstrating moderate effectiveness against A. clavatus and other fungi. In compound **8e**, the single fluorine substituent seems to counterbalance the electron-withdrawing effects and hydrophobic interactions. On the other hand, in compound **8c**, dual fluorine atoms may disrupt the optimal target interaction due to induced electronic distribution.

Table 1: Broad-spectrum Antimicrobial Profiling of Synthesized Compounds 8a-j

Compounds	MIC50 (µg/mL)	MIC90 (µg/mL)	GM-MIC (µg/mL)	MIC range (µg/mL)	Fold difference (Bacteria)	Fold difference (Fungi)
8a	200	1000	354.81	900.0	3.125	1.67
8b	125	1000	242.15	900.0	2.375	1.33
8c	250	1000	397.29	875.0	4.125	2.00
8d	125	1000	234.55	937.5	1.9375	1.67
8e	250	1000	276.02	875.0	3.125	1.33
8f	250	1000	348.55	800.0	4.5	1.33
8g	250	1000	305.78	900.0	3.75	1.33
8h	200	1000	268.26	900.0	2.5	1.67
8i	250	1000	285.93	900.0	2.875	1.67
8j	250	1000	315.69	900.0	4.0	1.33

Analysis of MIC50 values revealed compounds **8a**, **8b**, **8d** and **8h** exhibit broad-spectrum antimicrobial activity, achieving significant inhibition at lower concentrations. These findings are further corroborated by geometric mean MIC values, underscoring the consistent effectiveness of these compounds across both bacterial and fungal strains. The analysis of fold difference indicates that the synthesized compounds need about 1.9 to 4.1 times the concentration of chloramphenicol to achieve comparable antibacterial effectiveness. This highlights their potential as new antibacterial agents that can be further

improved. Moreover, several compounds display antifungal activity comparable to Griseofulvin, underscoring their potential as reliable antifungal agents.

The *in vitro* antimicrobial activity data demonstrate a clear structure-activity relationship (SAR), where electron-donating methyl groups enhance antibacterial properties, particularly against Gram-positive bacteria. Halogen substituents contribute variably, with their effects strongly influenced by their position on the aromatic ring, and fluorine-containing compounds showing moderate activity due to their unique electronic effects. Notably, compounds demonstrated higher activity against *C. albicans*, indicating a pronounced antifungal potential. These SAR insights emphasize the role of strategic substitution patterns in optimizing the indole-benzothiazole-1,2,3-triazole scaffold for enhanced antimicrobial properties, paving the way for future therapeutic development.

6.2.3 *In silico* studies: Multi-target docking against *C. albicans*

In this study, we used a multi-target molecular docking approach to analyze how synthesized hybrid compounds interact with five key proteins of *C. albicans*. The distinct chemical and biological properties of each moiety in these hybrid scaffolds enable effective targeting of different essential pathways in fungal metabolism and virulence. The hybrid nature of these compounds enables them to interact with multiple proteins, addressing different mechanisms of action, thus enhancing their potential as antifungal agents. Given this diversity in structural motifs, we targeted key proteins involved in different biological pathways of *C. albicans*: 14α-demethylase, Dihydrofolate reductase, Secreted aspartic proteases, Acetohydroxyacid synthase, and Enolase. By choosing these targets, we aimed to explore the multi-target potential of the hybrid compounds, ensuring that they can disrupt not just one, but several essential functions within the fungal cell. This approach aids in overcoming resistance mechanisms in fungi, which typically result from inhibiting a single target.

Table 2: Key Structural and Physicochemical Properties of Protein Binding Pockets

Descriptors	**Protein Pocket Properties**				
	1AI9	**1EAG**	**5V5Z**	**6DEQ**	**7V67**

Volume [Å^3]	1250.05	883.71	1353.07	1459.47	651.43
Surface [Å^2]	1566.78	972.52	1176.26	1378.92	746.76
Depth [Å]	30.13	21.93	35.34	21.22	23.13
Ellipsoid Ratio (c/a)	0.16	0.14	0.05	0.08	0.07
Ellipsoid Ratio (b/a)	0.19	0.42	0.20	0.23	0.33
Enclosure	0.14	0.19	0.03	0.06	0.13
Hydrophobicity Ratio	0.50	0.37	0.45	0.33	0.19
Apolar Amino acids Ratio	0.44	0.32	0.52	0.44	0.28
Polar Amino acid Ratio	0.35	0.44	0.33	0.41	0.42
Positive Amino acid Ratio	0.15	0.05	0.10	0.09	0.16
Negative Amino acid Ratio	0.07	0.20	0.03	0.06	0.14

The binding pocket properties of the targeted proteins, namely CYP51 (ergosterol biosynthesis, PDB ID: 5V5Z), DHFR (DNA synthesis, PDB ID: 1AI9), SAP (virulence factor, PDB ID: 1EAG), AHAS (amino acid biosynthesis, PDB ID: 6DEQ), and Enolase (glycolysis, PDB ID: 7V67), were systematically evaluated. The pocket descriptors, such as volume, surface area, depth, hydrophobicity ratio, and amino acid composition, as displayed in **Table 2**, played a crucial role in determining the specificity and stability of ligand binding. The protein binding pockets differed in shape and accessibility, with CYP51 having the most elongated and open structure for larger ligand accommodation. DHFR and SAP had moderately elongated, flexible pockets. In comparison, AHAS and

Enolase exhibited tighter but still accessible pocket structures, suggesting more intense ligand interactions. The binding pockets of the five targeted proteins are primarily composed of key residues including ALA, ARG, ASN, ASP, GLU, GLY, ILE, LEU, LYS, MET, PHE, PRO, SER, THR, TRP, TYR, and VAL, which facilitate a range of hydrophobic, electrostatic, and hydrogen-bonding interactions essential for ligand stability and binding. The docking outcomes, as summarized in **Table 3**, illustrate the binding energies (kcal/mol) of the synthesized compounds and the standard for each of the five proteins.

Table 3: Binding Energies (kcal/mol) of Synthesized Compounds Against Key Proteins in *C. albicans*

Sample	CYP51 (5V5Z)	DHFR (1AI9)	SAP (1EAG)	AHAS (6DEQ)	Enolase (7V67)
8a	-10.6	-9.8	-9.4	-11.3	-8.9
8d	-11.4	-9.6	-9.4	-10.8	-8.6
8f	-10.9	-9.7	-9.0	-10.8	-8.0
8h	-11.1	-10.4	-9.0	-10.9	-7.9
8i	-11.1	-8.7	-9.2	-11.0	-8.2
8j	-11.0	-9.5	-8.7	-10.3	-8.0
Griseofulvin	-7.6	-7.3	-6.6	-5.7	-6.5

The docking results highlight the efficacy of multi-target strategy, as **8a**, **8d**, and **8h** exhibit robust binding interactions with all five crucial proteins of *C. albicans*. The 2D and 3D visualizations of molecular docking **(Figure 3)** present a comprehensive depiction of the interactions between crucial residues in the protein binding pockets and the ligands. Notably, **8d** exhibits a high affinity of -11.4 kcal/mol towards CYP51, making it a compelling candidate for inhibiting ergosterol biosynthesis, a crucial pathway for preserving fungal cell membrane integrity. Moreover, its extensive range of effects is reinforced by its notable interactions with other proteins, including AHAS (-10.8 kcal/mol)

and DHFR (-9.6 kcal/mol), suggesting its capacity to impair crucial fungal pathways like amino acid biosynthesis and folate metabolism.

(a)

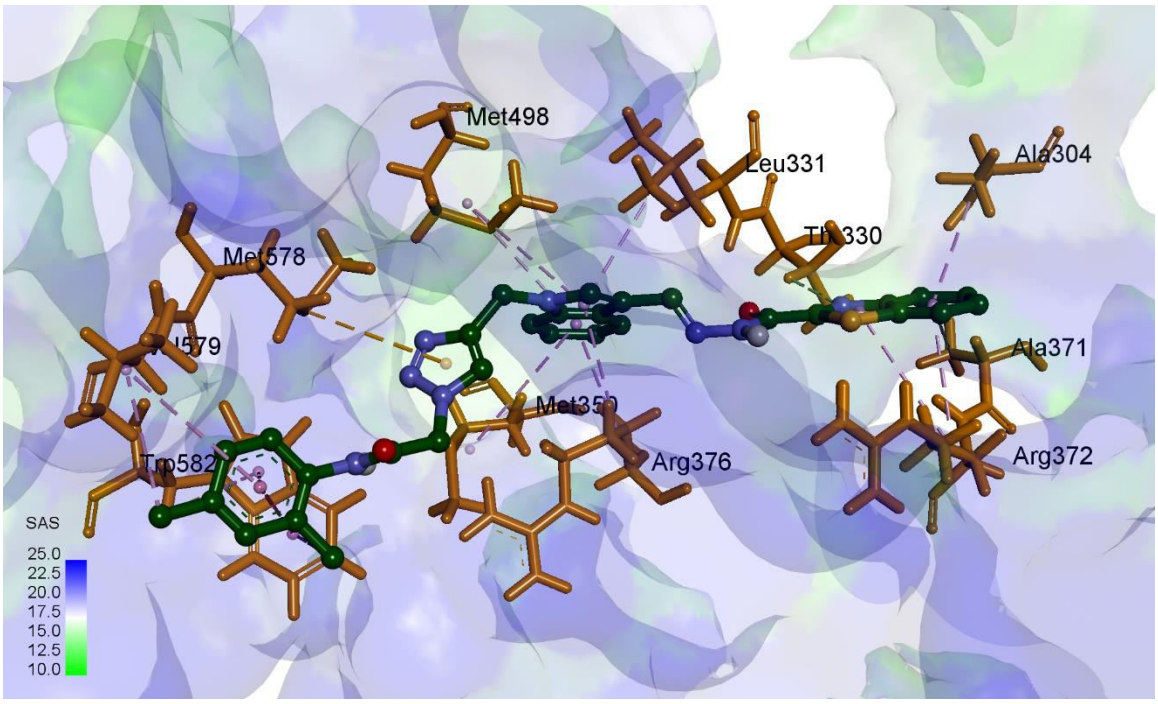

(b)

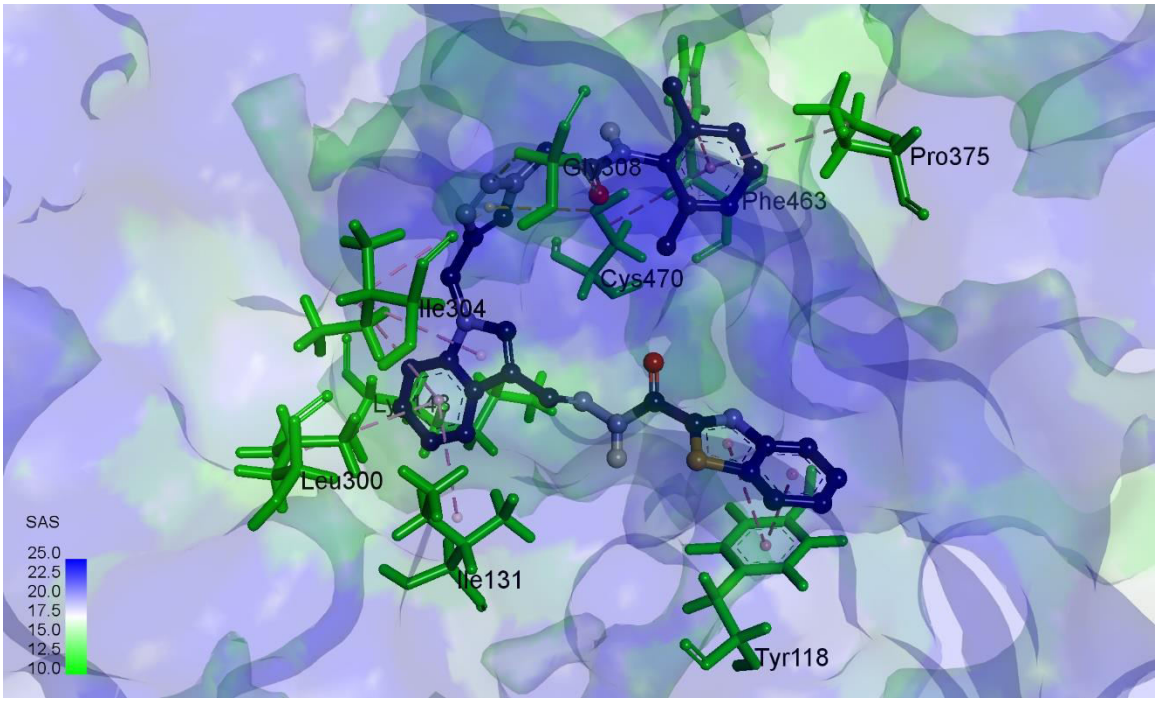

(c)

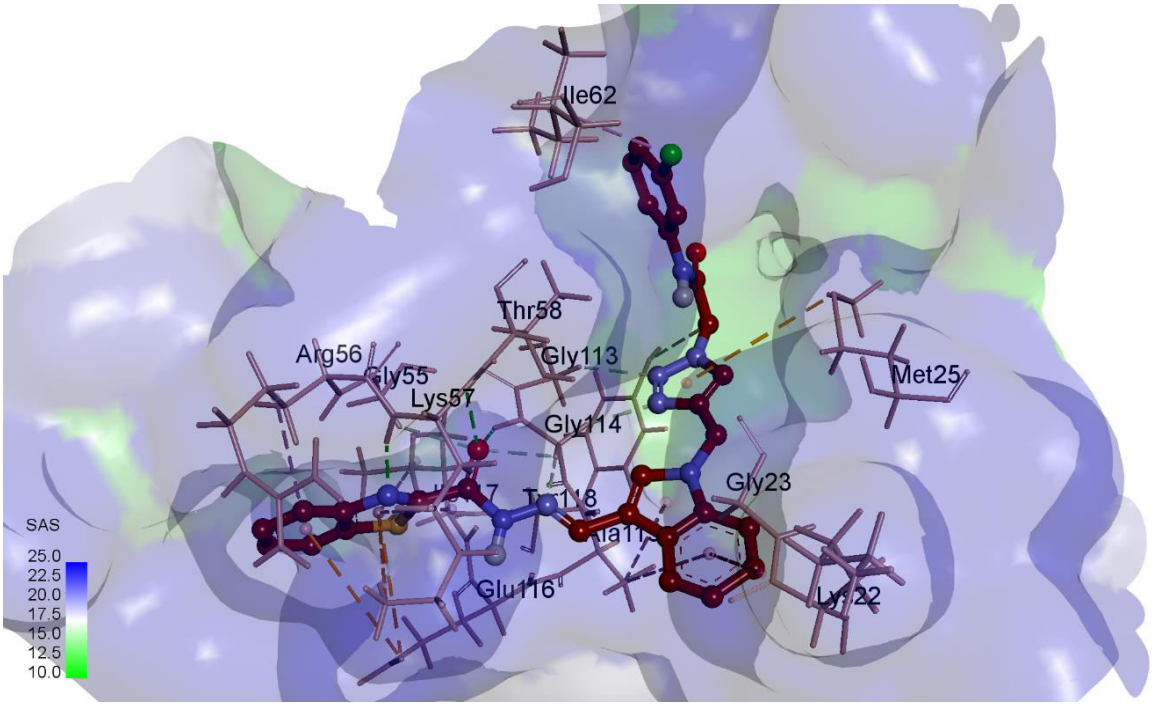
Ile62
Thr58
Arg56
Gly113
Met25
Lys57
Gly114
Gly23
Glu116
SAS
25.0
22.5
20.0
17.5
15.0
12.5
10.0

(d)

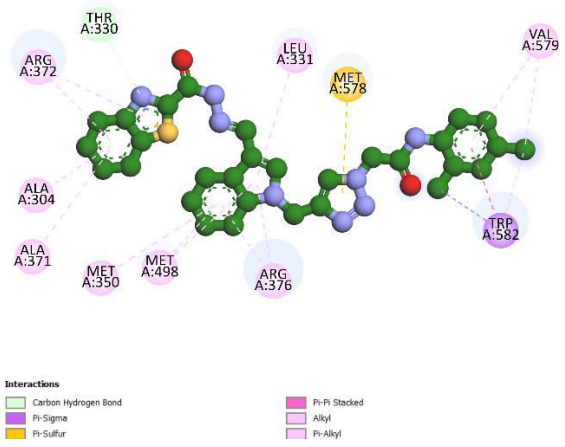
THR A:330
ARG A:372
LEU A:331
MET A:578
VAL A:579
ALA A:304
TRP A:582
ALA A:371
MET A:350
MET A:498
ARG A:376
Interactions
Carbon Hydrogen Bond
Pi-Sigma
Pi-Sulfur
Pi-Pi Stacked
Alkyl
Pi-Alkyl

(e)

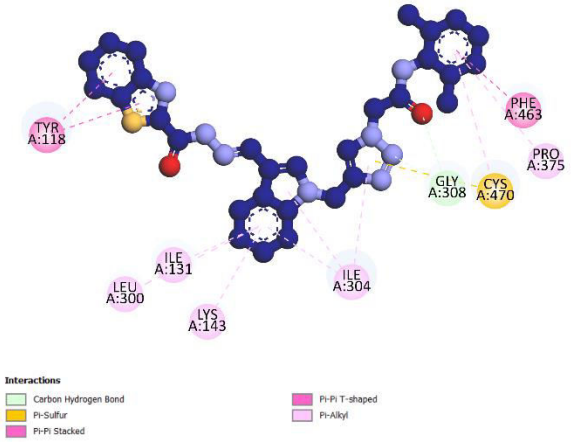
TYR A:118
PHE A:463
PRO A:375
GLY A:308
CYS A:470
ILE A:131
LEU A:300
ILE A:304
LYS A:143
Interactions
Carbon Hydrogen Bond
Pi-Sulfur
Pi-Pi Stacked
Pi-Pi T-shaped
Pi-Alkyl

(f)

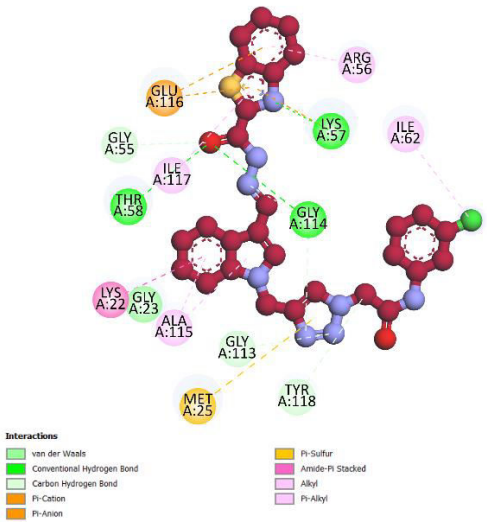

Figure 3: Molecular docking and interaction profiles of synthesized benzothiazole-triazole derivatives with their respective protein targets (a) 3D representation of compound 8a bound to the active site of protein 6DEQ, illustrating key interactions with amino acid residues (b) 3D representation of compound 8d docked into the active site of protein 5V5Z, highlighting hydrophobic and hydrogen bonding interactions (c) 3D interaction plot showing compound 8h within the binding site of protein 1AI9, emphasizing Pi-Pi stacked and conventional hydrogen bonds (d) 2D interaction plot for compound 8a with protein 6DEQ, illustrating the specific amino acid interactions such as Pi-Sulfur, Pi-Pi, and alkyl interactions (e) 2D interaction plot for compound 8d with protein 5V5Z, showing key hydrogen bond interactions and Pi-Alkyl contacts (f) 2D interaction plot for compound 8h bound to protein 1AI9 showing van der Waals interactions and amide-Pi stacked interactions that stabilize the binding

Similarly, **8h** displays remarkable affinity towards a range of targets. Among the compounds, **8h** exhibited the lowest binding energy toward DHFR (-10.4 kcal/mol), indicating its strong potential to inhibit folate metabolism, while it also demonstrated significant binding affinities for CYP51 (-11.1 kcal/mol) and AHAS (-10.9 kcal/mol), contributing to its broad-spectrum antifungal potential. Furthermore, **8a** demonstrates remarkable broad-spectrum capability. It exhibits a high affinity (-11.3 kcal/mol) for AHAS, which indicates a role in suppressing amino acid biosynthesis. Despite this, BIT-1 exhibits high affinity for other essential proteins like CYP51 (-10.6 kcal/mol) and DHFR (-9.8 kcal/mol), confirming its effectiveness as a broad-spectrum antifungal agent.

The presence of benzothiazole and triazole in these hybrid compounds likely had a major impact on their interactions with these crucial targets. The results indicate that hybrid

compounds with indole, benzothiazole, triazole, and acetamide scaffolds can target multiple pathways in *C. albicans*, effectively inhibiting its growth. The development of antifungal agents that inhibit multiple targets is helpful in addressing issues like drug resistance and narrow-spectrum activity associated with single-target drugs. Furthermore, the strong binding affinities observed for these compounds across all targets, especially compared to the reference drug griseofulvin, underscore their potential for development into more effective and broad-spectrum antifungal therapies. In summary, the use of hybrid compounds with diverse pharmacophores in a multi-target docking approach has resulted in the identification of potent inhibitors, including **8a**, **8d**, and **8h**, that effectively target multiple key proteins in *C. albicans*. This strategy improves antifungal efficacy and supports future development of next-gen antifungal agents for complex infections and drug resistance.

6.2.4 Molecular dynamics against selected proteins

In addition to the molecular docking studies, we conducted molecular dynamics (MD) simulations to evaluate the stability, flexibility, and interactions of the chosen hybrid compounds 8a (AHAS, PDB: 6DEQ), 8d (CYP51, PDB: 5V5Z), and 8h (DHFR, PDB: 1AI9) with their corresponding protein targets. To explore the dynamic behavior of the complexes, a 100 ns simulation was performed for each protein-ligand complex. The analysis encompassed various parameters such as root mean square deviation (RMSD), root mean square fluctuation (RMSF), radius of gyration (Rg), solvent-accessible surface area (SASA), and hydrogen bonding interactions.

8a with AHAS (6DEQ): The results from the MD simulation of the 8a-AHAS complex demonstrated a strong and stable interaction, as evidenced by the consistently low RMSD values of approximately 0.25 nm. These values indicate minimal structural deviations and support the conclusion that the protein-ligand complex is indeed stable. The Rg analysis provided additional evidence by showing stable values around 2.6 nm, confirming the protein's structural integrity. The RMSF data showed that specific loop regions had localized flexibility, but the key binding site residues remained stable, indicating strong interactions with **8a**. Throughout the simulation, the complex remained stable due to the consistent presence of 2–5 hydrogen bonds. The tight and well-protected binding site was

supported by the SASA values, which showed minimal solvent exposure and further confirmed the stable interaction.

(a)

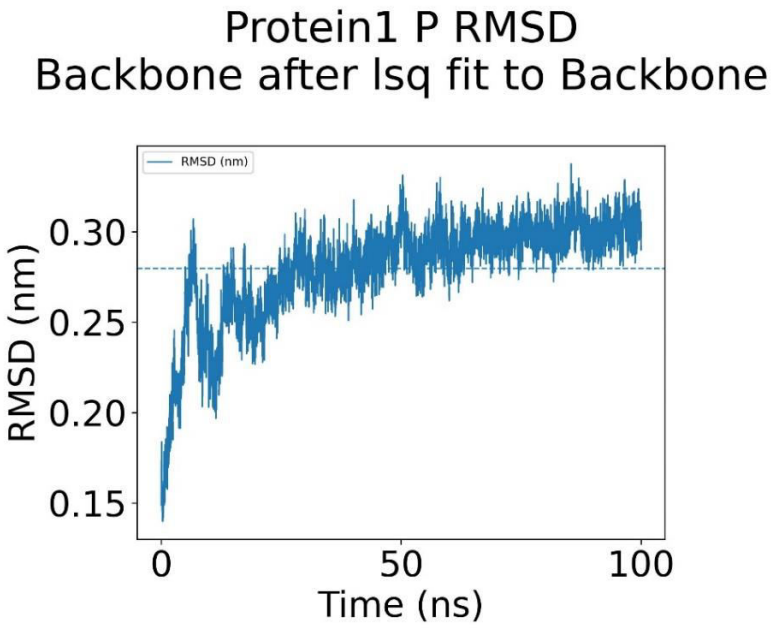

(b)

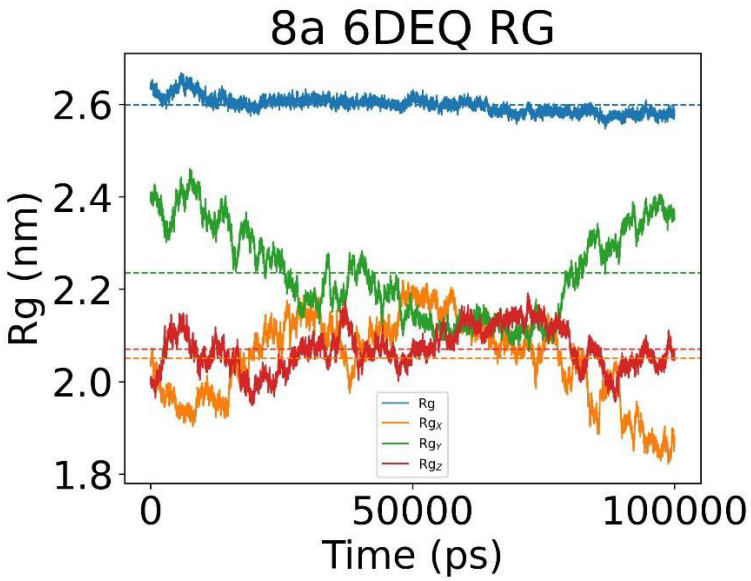

(c)

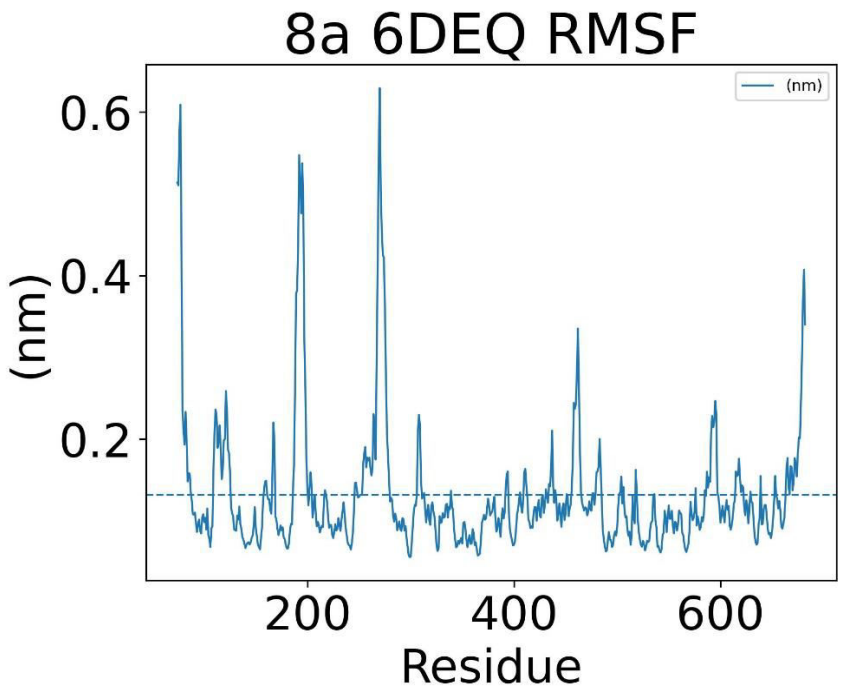
8a 6DEQ RMSF
(nm)
0.6
0.4
0.2
(nm)
200
400
600
Residue

(d)

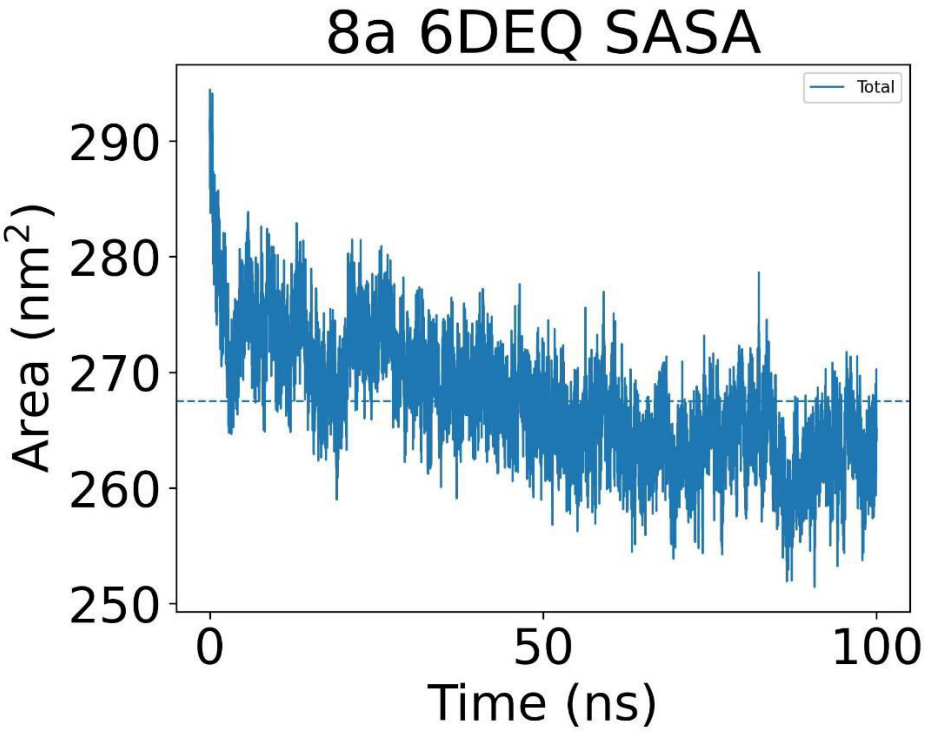
8a 6DEQ SASA
Total
290
280
270
260
250
Area (nm^2)
0
50
100
Time (ns)

(e)

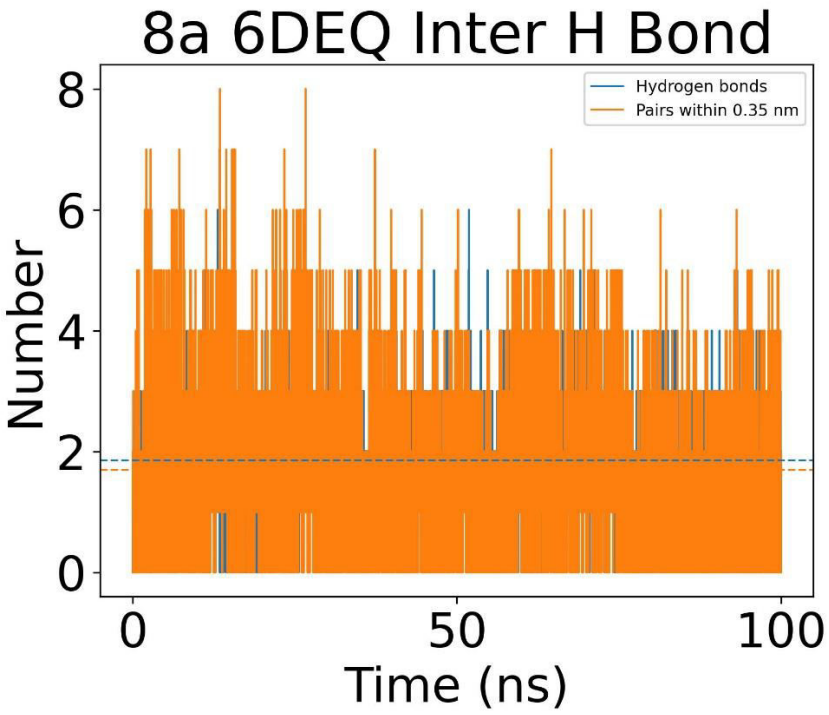

Figure 4: (a) RMSD plot for the backbone of the 8a-AHAS (6DEQ) complex, highlighting structural stability during the 100 ns simulation (b) Radius of gyration (Rg) of the 8a-AHAS (6DEQ) complex over the simulation time, indicating protein-ligand complex stability (c) RMSF of individual residues in AHAS (6DEQ) in the 8a complex, reflecting the flexibility of specific binding site residues (d) SASA plot for the 8a-AHAS (6DEQ) complex, showing solvent exposure dynamics during the 100 ns simulation (e) Hydrogen bond analysis of 8a with AHAS (6DEQ) during the 100 ns molecular dynamics simulation

8d with CYP51 (5V5Z): The MD simulation revealed that **8d**, a powerful binder to CYP51, maintained exceptional stability. The RMSD values showed fluctuations ranging from 0.25 to 0.40. The compactness of the complex was verified by the average Rg values of around 2.35 nm observed throughout the simulation. The RMSF analysis identified minimal fluctuations in the key binding residues, implying that the ligand formed strong and stable interactions with the protein. The examination of hydrogen bonding showed that 2-3 persistent hydrogen bonds were formed, playing a role in the stability of the ligand

within the binding pocket. Over the simulation period, the SASA values of **8d** indicated a decreasing trend, suggesting tighter binding within the CYP51 active site and reduced solvent exposure.

(a)

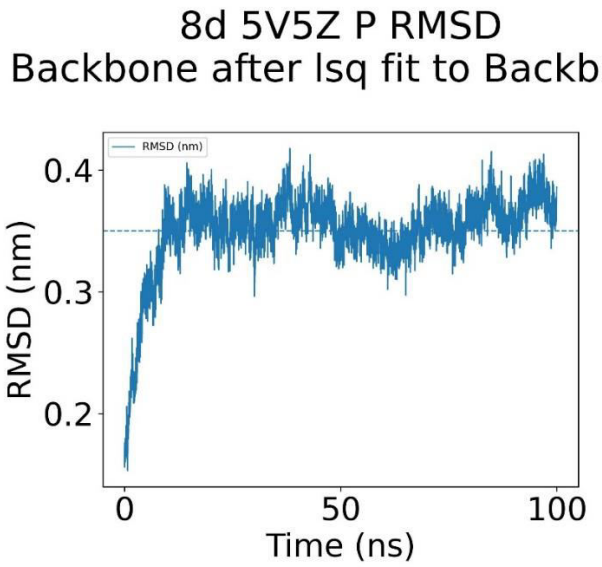

(b)

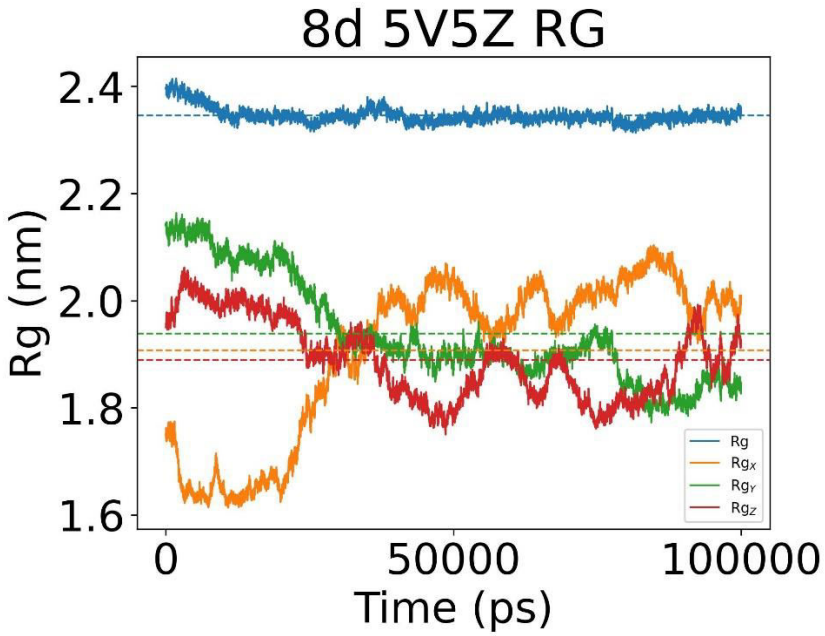

(c)

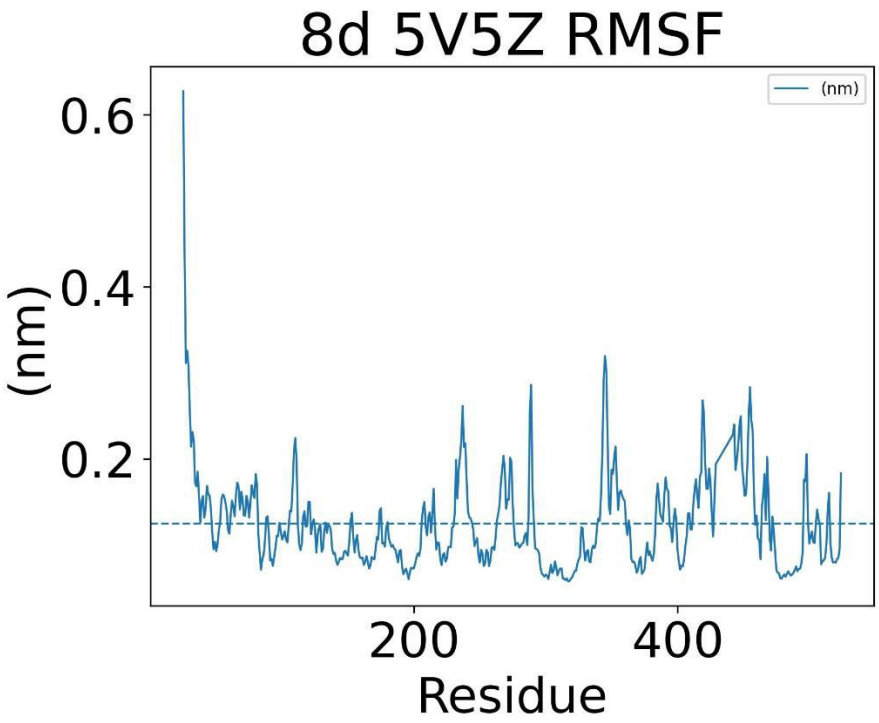
8d 5V5Z RMSF
(nm)
0.6
0.4
0.2
(nm)
200
400
Residue

(d)

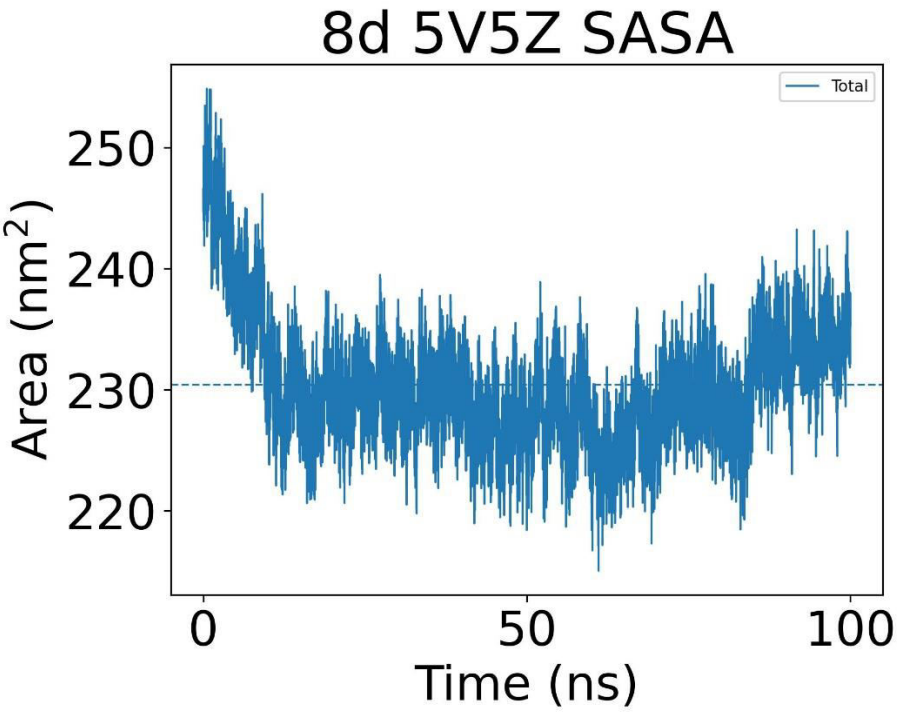
8d 5V5Z SASA
Total
250
240
230
220
Area (nm^2)
0
50
100
Time (ns)

(e)

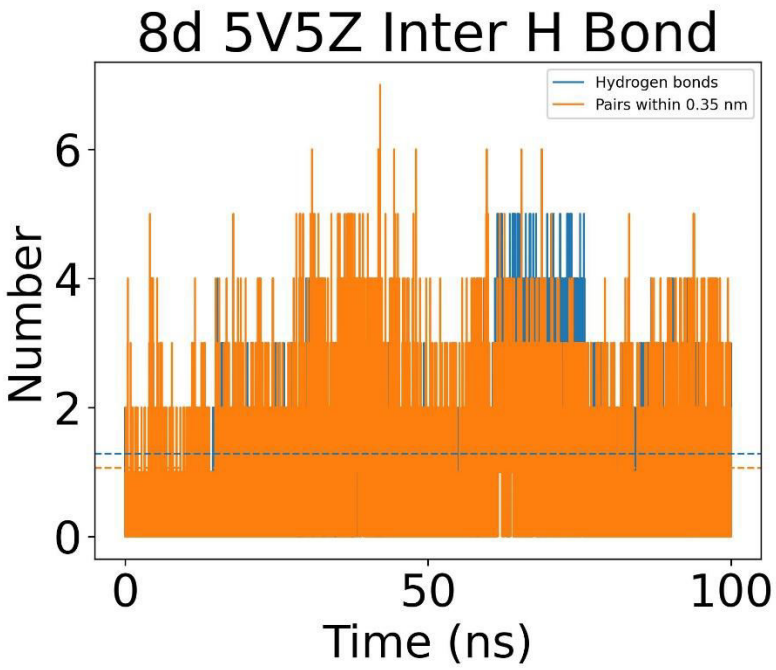

Figure 5: (a) RMSD of the backbone for 8d in complex with CYP51 (5V5Z), indicating structural stability throughout the simulation period (b) Radius of gyration (Rg) plot for the 8d-CYP51 (5V5Z) complex over the 100 ns simulation, depicting structural compactness Figure (c) RMSF of individual residues in the CYP51-8d complex, showing the flexibility of protein residues during the simulation. Figure (d) SASA profile for the 8d-CYP51 (5V5Z) complex over 100 ns, representing solvent exposure levels in the protein-ligand complex (e) Hydrogen bond analysis of 8d with CYP51 (5V5Z) during the 100 ns molecular dynamics simulation

8h with DHFR (1AI9): The RMSD profile of the 8h-DHFR complex remained stable during the entire 100 ns simulation. The RMSD values settled at around 0.25 nm following the initial equilibration, demonstrating a stable complex with minimal variations over time. The Rg values remained consistent around 1.65 nm, indicating the protein-ligand complex is compact. Furthermore, the RMSF analysis revealed minimal fluctuations in most protein residues, showing strong interactions between **8h** and the binding pocket residues. Through hydrogen bonding analysis, it was found that 2–4 stable hydrogen bonds existed during the simulation, contributing to the complex's stability. The SASA values remained steady

throughout the simulation, suggesting a stable binding interaction and minimal solvent exposure.

(a)

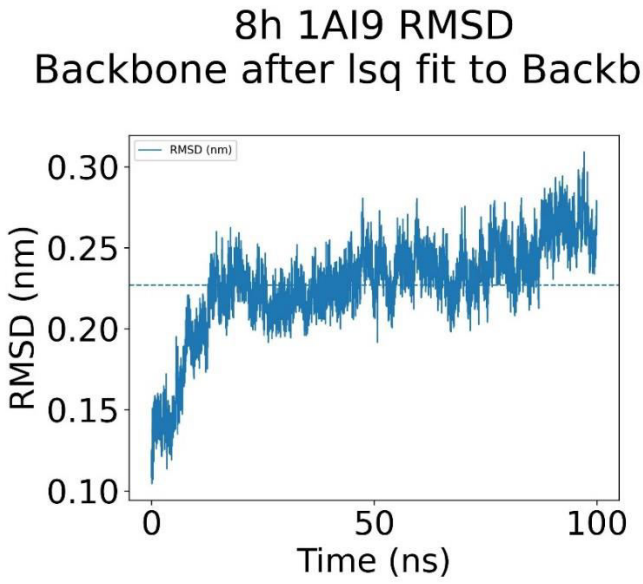

(b)

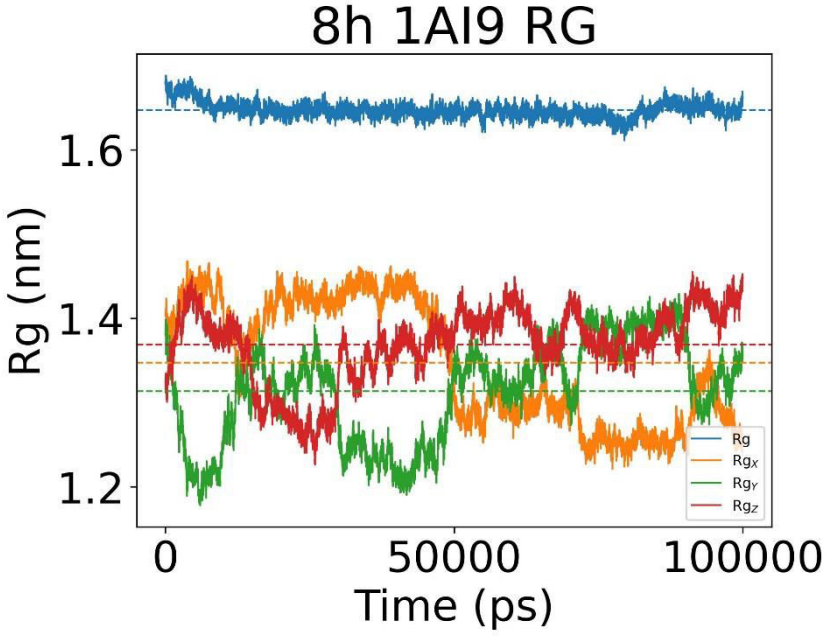

(c)

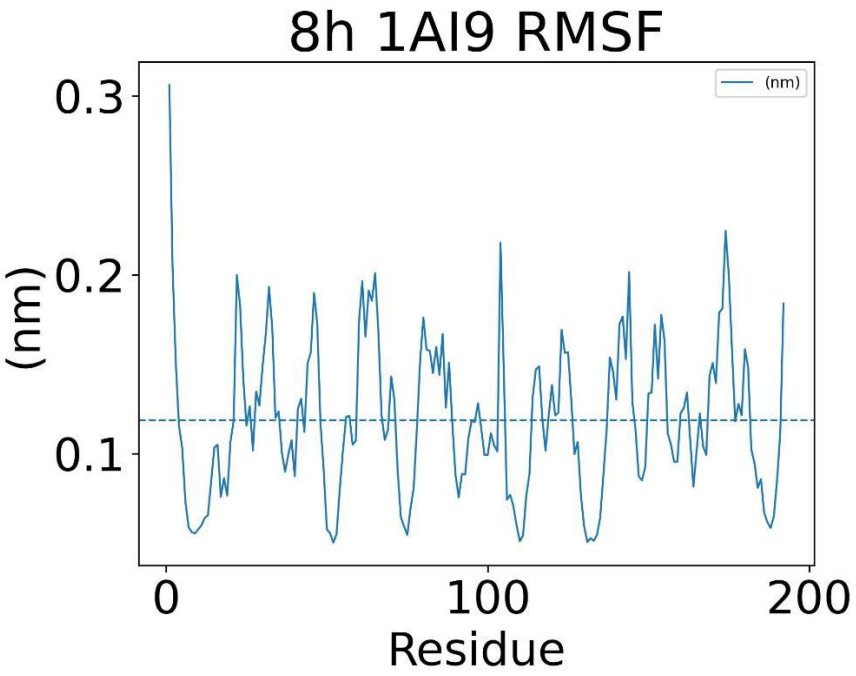
8h 1AI9 RMSF
(nm)
0.3
0.2
0.1
(nm)
0
100
200
Residue

(d)

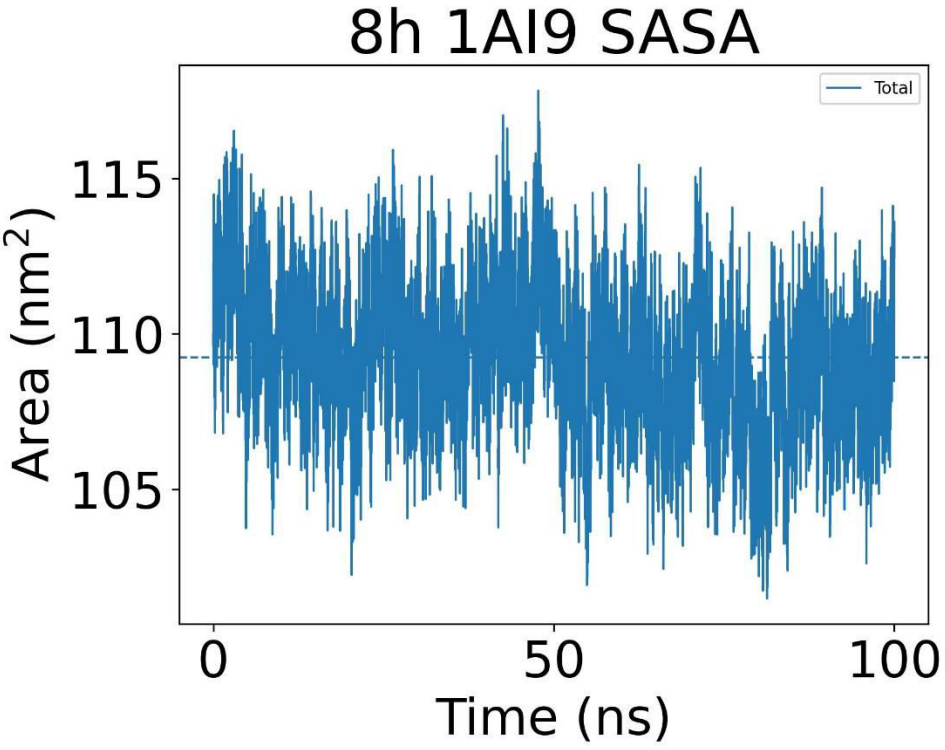
8h 1AI9 SASA
Total
115
110
105
Area (nm^2)
0
50
100
Time (ns)

(e)

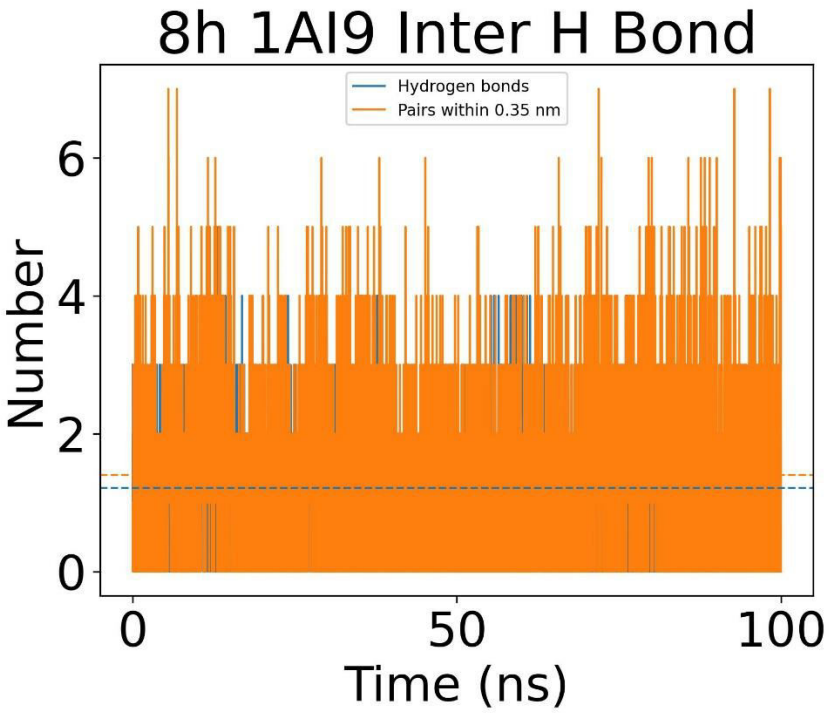

Figure 6: (a) Root mean square deviation (RMSD) of the backbone for 8h in complex with DHFR (1AI9), showing overall system stability over 100 ns (b) Radius of gyration (Rg) of the 8h-DHFR (1AI9) complex during the 100 ns simulation, indicating protein compactness (c) Root mean square fluctuation (RMSF) of individual residues of DHFR in the 8h complex, highlighting the flexibility of specific residues (d) Solvent accessible surface area (SASA) of the 8h-DHFR (1AI9) complex over the simulation time, representing the exposure of the ligand binding pocket to solvent (e) Hydrogen bond analysis of 8h with DHFR (1AI9) over a 100 ns molecular dynamics simulation

MM-PBSA calculations for the targeted protein-ligand complex:

MM-PBSA calculations were conducted to evaluate the binding free energies between the chosen compounds and their protein targets following molecular dynamics simulations. The results offer a deeper insight into the energy contributions affecting the stability of protein-ligand complexes.

6DEQ (Amino Acid Biosynthesis Inhibitor, 8a): The total binding energy was calculated as -155.317 kJ/mol, primarily driven by favorable van der Waals interactions (-309.966 kJ/mol). The electrostatic and polar solvation energies balance out, contributing to the overall stability of the complex.

5V5Z (CYP51 Inhibitor, 8d): The strongest binding energy observed was -232.340 kJ/mol, indicating a highly stable interaction with the protein. The favorable van der Waals energy (-347.219 kJ/mol) played a significant role, with additional contributions from electrostatics and solvation.

1AI9 (DHFR Inhibitor, 8h): The binding energy was -144.470 kJ/mol, showing moderate stability compared to the other complexes. The polar solvation and electrostatic contributions are higher here compared to the other targets, reflecting the protein's distinct binding environment.

Table 4: MM-PBSA Calculated Binding Energies and Energetic Contributions for the Protein-Ligand Complexes of 8a (6DEQ), 8d (5V5Z), and 8h (1AI9)

Descriptor	**8a-6DEQ**	**8d-5V5Z**	**8h-1AI9**
van der Waal Energy (kJ/mol)	-309.966 ± 13.379	-347.219 ± 10.221	-304.922 ± 12.869
Electrostatic Energy (kJ/mol)	-74.878 ± 11.484	-36.501 ± 11.122	-74.292 ± 15.845
Polar Solvation Energy (kJ/mol)	260.222 ± 22.564	183.880 ± 15.746	264.337 ± 21.725
SASA Energy (kJ/mol)	-30.695 ± 1.030	-32.501 ± 0.936	-29.592 ± 1.305
Binding Energy (kJ/mol)	-155.317 ± 14.788	-232.340 ± 14.039	-144.470 ± 26.395

The MM-PBSA outcomes shed light on the underlying mechanisms of protein-ligand interactions, showing that van der Waals forces are the primary driving force in all complexes. The robust binding energies, notably for 8d with 5V5Z, propose that these compounds possess the ability to act as effective inhibitors against C. albicans through multiple biological pathways. These results reinforce the potential of these hybrid compounds as antifungal agents, with strong binding affinities and stability across various proteins related to fungal virulence and metabolism.

6.3 Material and methods

6.3.1 Chemistry

In order to ensure accurate experimental results, all chemicals and reagents used in this research were of analytical grade and were used without any additional purification. Silica Gel 60 F_{254} TLC Aluminum Sheets (Merck KGaA, Darmstadt Germany) were employed for thin-layer chromatography, with the spots being visualized under UV light at 254 nm and 365 nm. The acquisition of the ^{1}H NMR and ^{13}C NMR spectra was performed on an AvanceNeo Ascend spectrometer operating at 400 MHz and 101 MHz respectively, utilizing DMSO-d_6 as the solvent. The chemical shifts are expressed in δ ppm and measured in relation to Tetramethyl silane (TMS) as the internal standard. For the mass spectral analysis, a Waters ACQUITY QDa spectrometer was used, which was operated using a direct inlet method. The Fourier Transform Infrared (FT-IR) spectrum was recorded using a Shimadzu FTIR-8400 spectrometer. The samples were prepared for infrared spectroscopy using the potassium bromide (KBr) pellet method. Using open capillaries, the melting points were recorded on an electrothermal device from Tempo instruments, and these values are uncorrected.

- **Synthesis protocol for 1-(prop-2-yn-1-yl)-1H-indole-3-carbaldehyde (2)**

The synthesis of compound **2** began with the reaction of indole-3-carbaldehyde **1** (15 mmol) and potassium carbonate (15 mmol) in dry DMF at room temperature, followed by stirring for 30 minutes. To this reaction mixture, propargyl bromide (15 mmol) was added, and the reaction was allowed to proceed for an additional 3 hours. Upon completion, as confirmed by TLC, the reaction mixture was poured into water, and the resulting precipitate

was collected by filtration. The solid was washed thoroughly with water to afford compound **2**.

- **General procedure for synthesis of 2-azido-N-phenylacetamide derivatives (5a-j)**

Aniline derivatives **3a-j** (10 mmol) were dissolved in acetone, followed by the addition of potassium carbonate (15 mmol). The mixture was stirred for 30 minutes to ensure complete dissolution. Chloroacetyl chloride (12 mmol) was then added dropwise to the stirred solution, and the reaction was allowed to proceed at room temperature for 3 hours, with completion monitored via thin-layer chromatography (TLC). Upon completion, the precipitate formed was collected by vacuum filtration, washed thoroughly with water, and dried. The resulting 2-chloro-N-phenylacetamide derivatives **4a-j** were obtained as solids and used directly in subsequent reactions without further purification. These derivatives **4a-j** were subsequently reacted with sodium azide (12 mmol) in DMF at room temperature for 6 hours. Upon completion, as confirmed by TLC, the reaction mixture was vacuum filtered, and the resulting compounds **5a-j** were used directly in subsequent reactions without further purification.

- **Standard procedure for synthesis of 2-(4-((3-formyl-1H-indol-1-yl)methyl)-1H-1,2,3-triazol-1-yl)-N-phenylacetamide derivatives (6a-j)**

Compound **2** (10 mmol) and derivatives **5a-j** (11 mmol) reacted using copper-catalyzed azide-alkyne cycloaddition (CuAAC). The reaction was catalyzed by $CuSO_4.5H_2O$ (4 mol%) and sodium ascorbate (2 mol%) in the reaction mixture. The reaction was stirred at room temperature for 12 hours. Upon completion, as confirmed by thin-layer chromatography (TLC), the mixture was poured into an aqueous solution of ammonium chloride to precipitate the intermediate product **6a-j**. The precipitate was collected, washed thoroughly with hot ethanol to obtain pure compounds **6a-j**, and dried for further use.

- **General procedure for synthesis of (E)-2-(4-((3-((2-(benzo[d]thiazole-2-carbonyl)hydrazineylidene)methyl)-1H-indol-1-yl)methyl)-1H-1,2,3-triazol-1-yl)-N-phenylacetamide derivatives (8a-j)**

The derivatives **6a-j** were dissolved in methanol, and 3-4 drops of glacial acetic acid were added to the solution. The mixture was stirred for 15 min, after which benzothiazole-2-hydrazide (10 mmol) was introduced. The reaction mixture was allowed to stir for an

additional 30 min. Upon completion, confirmed by TLC, the resulting precipitates were collected by filtration, washed with water, and further purified by washing with hot ethanol to yield the final derivatives **8a-j** as solid products.

- **(E)-2-(4-((3-((2-(benzo[d]thiazole-2-carbonyl)hydrazineylidene)methyl)-1H-indol-1-yl)methyl)-1H-1,2,3-triazol-1-yl)-N-(2,4-dimethylphenyl)acetamide (8a)**

Yield 92%; Reddish yellow; mp 173-175 °C; FT-IR (KBr, ν, cm^{-1}): 3286.81 (NH Stretch), 3255.95 (NH Stretch), 1666.55 (amide Stretch); ^{1}H NMR (400 MHz, DMSO) δ 12.46 (s, 1H, NH), 9.73 (s, 1H, NH), 8.88 (s, 1H, CH=N, indole), 8.37 (d, *J* = 7.7 Hz, 1H, Ar-H), 8.27-8.25 (d, *J* = 7.9 Hz, 1H, Ar-H), 8.22-8.20 (d, *J* = 9.0 Hz, 2H, Ar-H), 8.02 (s, 1H, CH, Indole), 7.74-7.72 (d, *J* = 8.1 Hz, 1H, Ar-H), 7.68-7.60 (dt, *J* = 25.0, 7.5 Hz, 2H, Ar-H, Thiazole), 7.29-7.22 (dq, *J* = 15.1, 7.3 Hz, 3H, Ar-H), 7.01 (s, 1H, Ar-H, Amide), 6.95 (d, *J* = 8.0 Hz, 1H, Ar-H), 5.59 (s, 2H, CH_2), 5.36 (s, 2H, CH_2), 2.22 (s, 3H, CH_3), 2.17 (s, 3H, CH_3); (ESI-MS) m/z 563.6 $(M+H)^+$; Anal. Calcd for $C_{30}H_{26}N_8O_2S$: C, 64.04; H, 4.66; N, 19.92; Found: C, 64.01; H, 4.62; N, 19.90%.

- **(E)-2-(4-((3-((2-(benzo[d]thiazole-2-carbonyl)hydrazineylidene)methyl)-1H-indol-1-yl)methyl)-1H-1,2,3-triazol-1-yl)-N-mesitylacetamide (8b)**

Yield 93%; Reddish yellow; mp 208-210 °C; FT-IR (KBr, ν, cm^{-1}): 3294.53 (NH Stretch), 3248.23 (NH Stretch), 1681.98 (amide Stretch); ^{1}H NMR (400 MHz, DMSO) δ 12.46 (s, 1H, NH), 9.68 (s, 1H, NH), 8.88 (s, 1H, CH=N, indole), 8.37-8.35 (d, *J* = 7.7 Hz, 1H, Ar-H), 8.27–8.20 (m, 3H, Ar-H), 8.01 (s, 1H, CH, Indole), 7.73-7.71 (d, *J* = 8.0 Hz, 1H, Ar-H), 7.66-7.60 (dt, *J* = 25.3, 7.5 Hz, 2H, Ar-H), 7.29-7.23 (dt, *J* = 22.5, 7.3 Hz, 2H, Ar-H), 6.85 (s, 2H, Ar-H), 5.58 (s, 2H, CH_2), 5.35 (s, 2H, CH_2), 2.19 (s, 3H, CH_3), 2.09 (s, 6H, CH_3); (ESI-MS) m/z 577.4 $(M + H)^+$; Anal. Calcd for $C_{31}H_{28}N_8O_2S$: C, 64.57; H, 4.89; N, 19.43; Found: C, 64.53; H, 4.87; N, 19.39%.

- **(E)-2-(4-((3-((2-(benzo[d]thiazole-2-carbonyl)hydrazineylidene)methyl)-1H-indol-1-yl)methyl)-1H-1,2,3-triazol-1-yl)-N-(2,6-difluorophenyl)acetamide (8c)**

Yield 84%; Reddish yellow; mp 210-212 °C; FT-IR (KBr, ν, cm^{-1}): 3309.96 (NH Stretch), 3225.09 (NH Stretch), 1681.98 (amide Stretch); ^{1}H NMR (400 MHz, DMSO) δ 12.45 (s, 1H, NH), 10.31 (s, 1H, NH), 8.86 (s, 1H, CH=N, indole), 8.35-8.34 (d, *J* = 7.8 Hz, 1H, Ar-

H), 8.27–8.20 (m, 3H, Ar-H), 8.01 (s, 1H, CH, Indole), 7.73-7.58 (ddd, *J* = 32.1, 17.5, 7.8 Hz, 3H,Ar-H), 7.38–7.36 (m, 1H), 7.34–7.15 (m, 4H), 5.59 (s, 2H, CH_2), 5.45 (s, 2H, CH_2); (ESI-MS) m/z 571.2 $(M + H)^+$; Anal. Calcd for $C_{28}H_{20}F_2N_8O_2S$: C, 58.94; H, 3.53; N, 19.64; Found: C, 58.90; H, 3.52; N, 19.63%.

- **(E)-2-(4-((3-((2-(benzo[d]thiazole-2-carbonyl)hydrazineylidene)methyl)-1H-indol-1-yl)methyl)-1H-1,2,3-triazol-1-yl)-N-(2,6-dimethylphenyl)acetamide (8d)**

Yield 93%; Reddish yellow; mp 198-200 °C; FT-IR (KBr, ν, cm^{-1}): 3294.53 (NH Stretch), 3248.23 (NH Stretch), 1658.84 (amide Stretch); ^1H NMR (400 MHz, DMSO) δ 12.46 (s, 1H, NH), 9.78 (s, 1H, NH), 8.88 (s, 1H, CH=N, indole), 8.38-8.36 (d, *J* = 7.8 Hz, 1H, Ar-H), 8.26 – 8.21 (m, 3H, Ar-H), 8.02 (s, 1H, CH, Indole), 7.73-7.72 (d, *J* = 8.1 Hz, 1H, Ar-H), 7.66-7.64 (t, *J* = 7.5 Hz, 1H, Ar-H), 7.61-7.59 (d, *J* = 7.8 Hz, 1H, Ar-H), 7.29-7.24 (dt, *J* = 22.9, 7.3 Hz, 2H, Ar-H), 7.06 (s, 3H, Ar-H), 5.59 (s, 2H, CH_2), 5.39 (s, 2H, CH_2), 2.15 (s, 6H CH_3); (ESI-MS) m/z 563.3 $(M + H)^+$; Anal. Calcd for $C_{30}H_{26}N_8O_2S$: C, 64.04; H, 4.66; N, 19.92; Found: C, 64.03; H, 4.62; N, 19.91%.

- **(E)-2-(4-((3-((2-(benzo[d]thiazole-2-carbonyl)hydrazineylidene)methyl)-1H-indol-1-yl)methyl)-1H-1,2,3-triazol-1-yl)-N-(4-fluorophenyl)acetamide (8e)**

Yield 87%; Reddish yellow; mp 190-192 °C; FT-IR (KBr, ν, cm^{-1}): 3286.81 (NH Stretch), 1666.55 (amide Stretch); ^1H NMR (400 MHz, DMSO) δ 12.47 (s, 1H, NH), 10.56 (s, 1H, NH), 8.90 (s, 1H, CH=N, indole), 8.43 (d, *J* = 7.7 Hz, 1H,Ar-H), 8.37-8.36 (d, *J* = 7.6 Hz, 1H, Ar-H),8.26-8.21 (d, *J* = 7.9 Hz, 2H, Ar-H), 8.03 (s, 1H, CH, Indole), 7.74 (d, *J* = 8.1 Hz, 1H, Ar-H), 7.72 – 7.61 (m, 4H, Ar-H), 7.29-7.22 (dt, *J* = 24.3, 7.3 Hz, 2H), 7.17-7.15 (t, *J* = 8.6 Hz, 2H), 5.60 (s, 2H, CH_2), 5.35 (s, 2H, CH_2); (ESI-MS) m/z 553.1 $(M + H)^+$; Anal. Calcd for $C_{28}H_{21}FN_8O_2S$: C, 60.86; H, 3.83; N, 20.28; Found: C, 60.84; H, 3.79; N, 20.24%.

- **(E)-2-(4-((3-((2-(benzo[d]thiazole-2-carbonyl)hydrazineylidene)methyl)-1H-indol-1-yl)methyl)-1H-1,2,3-triazol-1-yl)-N-(4-chlorophenyl)acetamide (8f)**

Yield 89%; Reddish yellow; mp 212-214 °C; FT-IR (KBr, ν, cm^{-1}): 3279.10 (NH Stretch), 1666.55 (amide Stretch); ^1H NMR (400 MHz, DMSO) δ 12.45 (s, 1H, NH), 10.61 (s, 1H, NH), 8.86 (s, 1H, CH=N, indole), 8.34-8.32 (d, *J* = 7.8 Hz, 1H, Ar-H), 8.27-8.25 (d, *J* = 7.9 Hz, 1H, Ar-H), 8.21-8.19 (d, *J* = 10.6 Hz, 2H, Ar-H), 8.02 (s, 1H, CH, Indole), 7.73-

7.71 (d, *J* = 8.1 Hz, 1H, Ar-H), 7.68-7.64 (t, *J* = 7.6 Hz, 1H), 7.61-7.59 (dd, *J* = 8.6, 3.7 Hz, 3H, Ar-H), 7.39-7.37 (d, *J* = 8.4 Hz, 2H, Ar-H), 7.31-7.25 (dt, *J* = 24.4, 7.3 Hz, 2H, Ar-H), 5.60 (s, 2H, CH_2), 5.34 (s, 2H, CH_2); ^{13}C NMR DEPT-135 (101 MHz, DMSO) δ 147.33 (CH=N), 134.16 (CH, indole), 129.29, 127.64, 127.36, 125.78, 124.45, 123.47, 122.70, 121.57, 121.24, 111.28 (Ar-C), 52.71 (CH_2), 41.56 (CH_2); (ESI-MS) m/z 571.1 (M + H)$^+$; Anal. Calcd for $C_{28}H_{21}ClN_8O_2S$: C, 59.10; H, 3.72; N, 19.69; Found: C, 59.09; H, 3.71; N, 19.67%.

- **(E)-2-(4-((3-((2-(benzo[d]thiazole-2-carbonyl)hydrazineylidene)methyl)-1H-indol-1-yl)methyl)-1H-1,2,3-triazol-1-yl)-N-(4-bromophenyl)acetamide (8g)**

Yield 82%; Reddish yellow; mp 193-195 °C; FT-IR (KBr, ν, cm^{-1}): 3286.81 (NH Stretch), 1674.27 (amide Stretch); ^{1}H NMR (400 MHz, DMSO) δ 12.45 (s, 1H, NH), 10.62 (s, 1H, NH), 8.87 (s, 1H, CH=N, indole), 8.35-8.33 (d, *J* = 7.7 Hz, 1H, Ar-H), 8.27 (d, *J* = 7.8 Hz, 1H, Ar-H), 8.25-8.19 (d, *J* = 8.1 Hz, 2H, Ar-H), 8.02 (s, 1H, CH, Indole), 7.73-7.71 (d, *J* = 8.1 Hz, 1H, Ar-H), 7.67 – 7.60 (m, 3H, Ar-H), 7.57-7.57 (d, *J* = 8.6 Hz, 3H), 7.31-7.21 (dt, *J* = 24.2, 7.3 Hz, 2H), 5.59 (s, 2H, CH_2), 5.34 (s, 2H, CH_2); (ESI-MS) m/z 613.49 (M + H)$^+$; Anal. Calcd for $C_{28}H_{21}BrN_8O_2S$: C, 54.82; H, 3.45; N, 18.27: Found: C, 54.79; H, 3.44; N, 18.26%.

- **(E)-2-(4-((3-((2-(benzo[d]thiazole-2-carbonyl)hydrazineylidene)methyl)-1H-indol-1-yl)methyl)-1H-1,2,3-triazol-1-yl)-N-(3-chlorophenyl)acetamide (8h)**

Yield 85%; Reddish yellow; mp 170-172 °C; FT-IR (KBr, ν, cm^{-1}): 3271.38 (NH Stretch), 1666.55 (amide Stretch); ^{1}H NMR (400 MHz, DMSO) δ 12.46 (s, 1H, NH), 10.68 (s, 1H, NH), 8.88 (s, 1H, CH=N, indole), 8.37-8.35 (d, *J* = 7.7 Hz, 1H, Ar-H), 8.26-8.24 (d, *J* = 7.6 Hz, 1H, Ar-H), 8.21 (d, *J* = 6.1 Hz, 2H, Ar-H), 8.03 (s, 1H, CH, Indole), 7.78 (s, 1H, Ar-H), 7.74-7.72 (d, *J* = 8.0 Hz, 1H, Ar-H), 7.65-7.59 (dt, *J* = 24.8, 7.4 Hz, 2H, Ar-H), 7.45-7.44 (d, *J* = 8.1 Hz, 1H, Ar-H), 7.37-7.22 (ddd, *J* = 32.6, 16.8, 7.8 Hz, 3H, Ar-H), 7.14-7.13 (d, *J* = 7.8 Hz, 1H, Ar-H), 5.61 (s, 2H, CH_2), 5.37 (s, 2H, CH_2); (ESI-MS) m/z 570.1 (M + H)$^+$; Anal. Calcd for $C_{28}H_{21}ClN_8O_2S$: C, 59.10; H, 3.72; N, 19.69; Found: C, 59.05; H, 3.70; N, 19.64%.

- **(E)-2-(4-((3-((2-(benzo[d]thiazole-2-carbonyl)hydrazineylidene)methyl)-1H-indol-1-yl)methyl)-1H-1,2,3-triazol-1-yl)-N-(p-tolyl)acetamide (8i)**

Yield 90%; Reddish yellow; mp 210-212 °C; FT-IR (KBr, ν, cm^{-1}): 3367.17 (NH Stretch), 1674.27 (amide Stretch); ^{1}H NMR (400 MHz, DMSO) δ 12.45 (s, 1H, NH), 10.38 (s, 1H, NH), 8.86 (s, 1H, CH=N, indole), 8.34-8.33 (d, *J* = 7.7 Hz, 1H, Ar-H), 8.27-8.25 (d, *J* = 7.9 Hz, 1H), 8.21 – 8.18 (m, 2H, Ar-H), 8.01 (s, 1H, CH, Indole), 7.73-7.71 (d, *J* = 8.1 Hz, 1H, Ar-H), 7.68-7.58 (dt, *J* = 23.8, 7.5 Hz, 2H, Ar-H), 7.47-7.45 (d, *J* = 8.0 Hz, 2H, Ar-H), 7.31-7.21 (dt, *J* = 24.4, 7.3 Hz, 2H, Ar-H), 7.13-7.10 (d, *J* = 8.0 Hz, 2H, Ar-H), 5.59 (s, 2H, CH_2), 5.35 (s, 2H, CH_2), 2.24 (s, 3H, CH_3); (ESI-MS) m/z 549.2 $(M + H)^+$; Anal. Calcd for $C_{29}H_{24}N_8O_2S$: C, 63.49; H, 4.41; N, 20.42; Found: C, 63.48; H, 4.39; N, 20.41%.

- **(E)-2-(4-((3-((2-(benzo[d]thiazole-2-carbonyl)hydrazineylidene)methyl)-1H-indol-1-yl)methyl)-1H-1,2,3-triazol-1-yl)-N-(4-methoxyphenyl)acetamide (8j)**

Yield 89%; Reddish yellow; mp 196-198 °C; FT-IR (KBr, ν, cm^{-1}): 3379.10 (NH Stretch), 1666.55 (amide Stretch); ^{1}H NMR (400 MHz, DMSO) δ 12.45 (s, 1H, NH), 10.34 (s, 1H,NH), 8.86 (s, 1H, CH=N, indole), 8.35-8.33 (d, *J* = 7.7 Hz, 1H, Ar-H), 8.27-8.25 (d, *J* = 7.9 Hz, 1H, Ar-H), 8.21-8.19 (d, *J* = 9.5 Hz, 2H, Ar-H), 8.02 (s, 1H, CH, Indole), 7.73-7.71 (d, *J* = 8.1 Hz, 1H, Ar-H), 7.68-7.58 (dt, *J* = 24.1, 7.4 Hz, 2H, Ar-H), 7.50-7.48 (d, *J* = 8.5 Hz, 2H, Ar-H), 7.31-7.21 (dt, *J* = 24.3, 7.3 Hz, 2H, Ar-H), 6.91-6.88 (d, *J* = 8.6 Hz, 2H, Ar-H), 5.59 (s, 2H, CH_2), 5.29 (s, 2H, CH_2), 3.71 (s, 3H, OCH_3); (ESI-MS) m/z 565.3 $(M + H)^+$; Anal. Calcd for $C_{29}H_{24}N_8O_3S$: C, 61.69; H, 4.28; N, 19.85; Found: C, 61.68; H, 4.28; N, 19.83%.

6.3.2 *In vitro* minimum inhibition concentration procedure

The synthesized compounds were subjected to assessment of their antimicrobial activity using the micro broth dilution method.[258] To ensure sterility, all glassware was thoroughly sterilized before testing. The compounds were screened against a panel of standard bacterial and fungal strains, including Escherichia coli (MTCC–443), Pseudomonas aeruginosa (MTCC–1688), Staphylococcus aureus (MTCC–96), Streptococcus pyogenes (MTCC–442), Acinetobacter baumannii (MTCC–12890), Candida albicans (MTCC–227), Aspergillus niger (MTCC–282), and Aspergillus clavatus (MTCC–1323). In order to conduct the research, we acquired all the microbial strains from the Microbial Type Culture Collection (MTCC) housed at the Institute of Microbial Technology in Chandigarh. The nutrient medium used for bacterial cultures, Mueller Hinton Broth, was selected to aid in compound dilution, whereas Sabouraud Dextrose

Broth was specifically employed for fungal cultures. In order to ensure consistency, the turbidity was adjusted to achieve a standardized inoculum size of 10^8 CFU/mL for all microbial strains. In order to achieve the necessary concentrations, the test compounds were diluted using dimethyl sulfoxide (DMSO) as a solvent. The initial screening process began by preparing a stock solution of each compound at a concentration of 2000 µg/mL. This was then followed by serial dilutions to obtain concentrations of 1000 µg/mL, 500 µg/mL, and 250 µg/mL. Following the initial screening, the active compounds underwent a secondary screening process where they were tested at various concentrations, including 200 µg/mL, 100 µg/mL, 50 µg/mL, 25 µg/mL, 12.5 µg/mL, and 6.25 µg/mL. To ensure precision, a control group was included in every test, which did not contain any antibiotic. Following a 24-hour incubation period at a temperature of 37°C, the concentration at which no observable microbial growth was seen, in comparison to the control, was designated as the minimum inhibitory concentration (MIC). Additional subculturing was done on the tubes that did not show any visible growth in order to verify that there was indeed no growth. The highest dilution that demonstrated at least 99% inhibition was recorded as the final results. In order to ensure the accuracy of the method, control organisms were included in the testing process. Additionally, a second set of tests was conducted where an organism with a known sensitivity was introduced to validate the screening results.

6.3.3 In silico Molecular docking method

The protein structures were obtained from the RCSB Protein Data Bank (PDB), with selected targets including CYP51 (PDB ID: 5V5Z), DHFR (PDB ID: 1AI9), SAP (PDB ID: 1EAG), AHAS (PDB ID: 6DEQ), and Enolase (PDB ID: 7V67). The removal of all water molecules and heteroatoms from these structures was carried out using UCSF Chimera (version 1.17.3) as part of the preparation process for the multi-target docking approach.[210] In order to ensure the structural completeness of the protein, the Dunbrack 2010 rotamer library was used alongside the Chimera's Dock Prep tool for protein preparation.[211] This involved reconstructing incomplete side chains. The addition of hydrogen atoms was done to optimize the protein geometry, ensuring accurate interaction modeling. Moreover, the assignment of electrostatic charges was carried out using the AMBER ff14SB force field for standard residues and AM1-BCC for non-standard

residues, thus facilitating precise electrostatic interactions. Through the ACPYPE server, the ligands were carefully optimized and prepared for docking.[212] To ensure precise conformational accuracy, the AMBER method was utilized, along with bcc charge assignments. To conduct the docking simulations, we utilized AutoDock Vina 1.5.7, which was seamlessly integrated as an extension in UCSF Chimera. The parameters for ligand generation were configured to produce a maximum of 10 binding modes per ligand. These settings included an exhaustiveness value of 8 and a maximum energy difference of 3 kcal/mol between the poses. The utilization of BIOVIA Discovery Studio Visualizer 2024 facilitated the analysis and visualization of the top-ranked docking poses, enabling a thorough investigation of the ligand-protein interactions within the multi-target docking approach.[213]

6.3.4 Molecular dynamics simulation

The GROMACS 2019.4 software package was used to conduct molecular dynamics (MD) simulations. [215] In order to obtain precise force field parameters, the ligand topology was created using the Automated Topology Builder (ATB) server. [216] The system underwent vacuum minimization by employing the steepest descent algorithm for 1500 steps as part of its preparation. To ensure proper solvation of the protein-ligand complex, a cubic periodic box was utilized with a distance of 0.5 nm between the complex and the edges of the box. The solvation was carried out using the simple point charge (SPC) water model. The addition of 0.15 M Na^+ and Cl^- ions was done with the aim of neutralizing the system and reaching a physiological salt concentration. The system preparation process was carried out in accordance with the methodology outlined in a study that was previously published (PMID: 31514687). Following the equilibration process in the NPT ensemble, the final production run was carried out for a duration of 100 ns under the same isothermal-isobaric conditions. The GROMACS simulation tools were utilized to perform trajectory analysis, which involved assessing various parameters including root mean square deviation (RMSD), root mean square fluctuation (RMSF), radius of gyration (Rg), solvent-accessible surface area (SASA), and hydrogen bond interactions. The analysis procedures that were used in this study followed established protocols that were previously documented in a study with the PMID: 32567989.

6.4 conclusion

In the course of this study, we have effectively synthesized a range of hybrid compounds that incorporate indole, benzothiazole, triazole, and acetamide elements. These compounds have been thoroughly examined to determine their potential antifungal and antibacterial properties. Through the implementation of a multi-target molecular docking approach, it became evident that these hybrids possess the capability to interact with multiple key proteins in C. albicans. This impressive list of proteins includes CYP51, DHFR, SAP, AHAS, and Enolase, indicating that their mechanism of action is broad-spectrum in nature. The results of experiment point out that compounds 8a, 8d, and 8h displayed the highest binding affinities. This finding implies their significant role in inhibiting key biological pathways, namely ergosterol biosynthesis, DNA synthesis, and amino acid biosynthesis. The stability and robust interactions of these compounds with their target proteins were further validated through molecular dynamics simulations. Additionally, MM-PBSA calculations confirmed favorable binding energies, providing additional evidence to support the promising drug-likeness of the selected compounds. These hybrids have proven to be highly effective, especially in their ability to combat Candida albicans. This discovery emphasizes their potential as next-generation antifungal agents, offering a broad range of efficacy and the ability to overcome common drug resistance mechanisms. These results serve as a solid groundwork for future research in both in vitro and in vivo settings, signifying a notable progression in the development of antifungal drugs.

6.5 spectral data

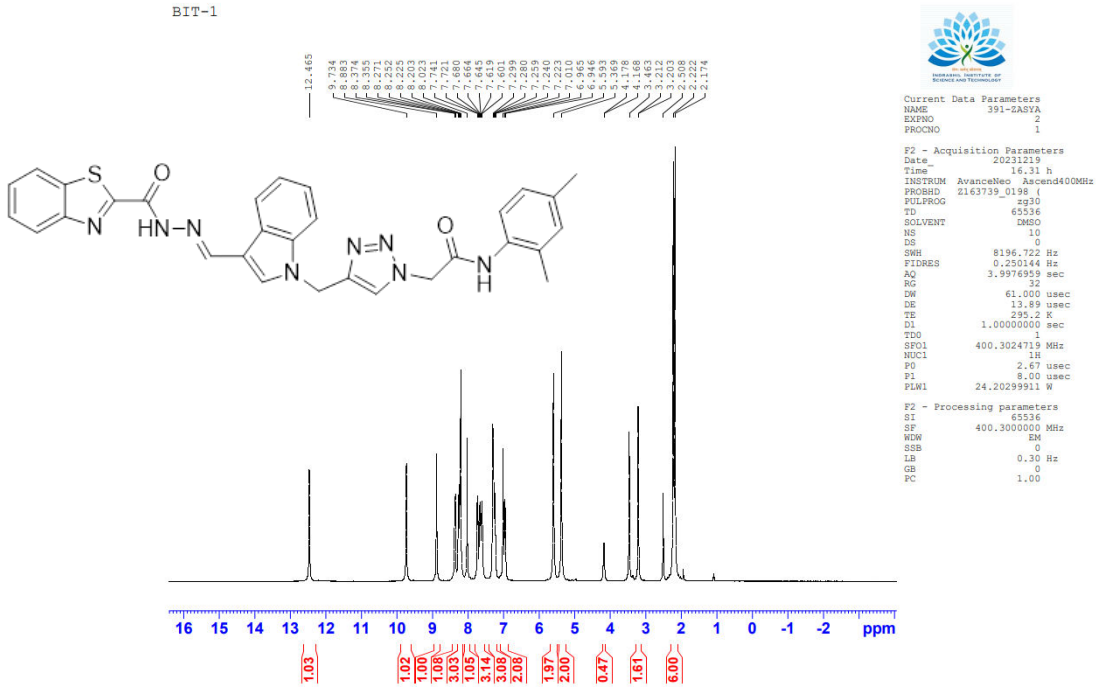

Figure 7: Representative ^{1}H NMR spectrum of compound 8a

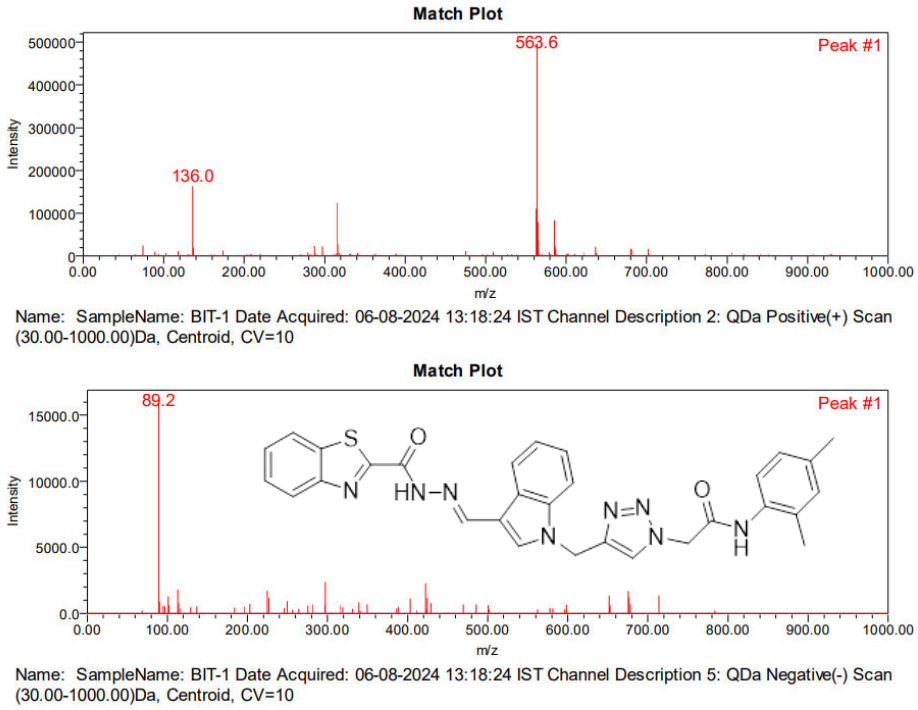

Figure 8: Representative mass spectrum of compound 8a

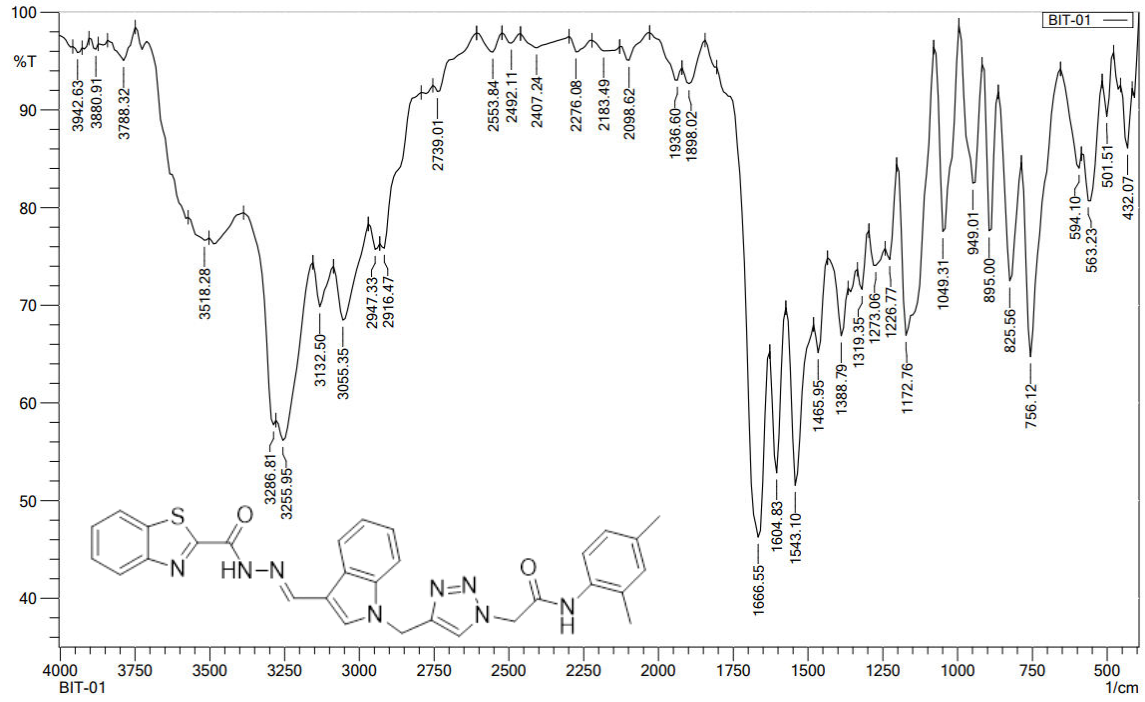

Figure 9: Representative FT-IR spectrum of compound 8a

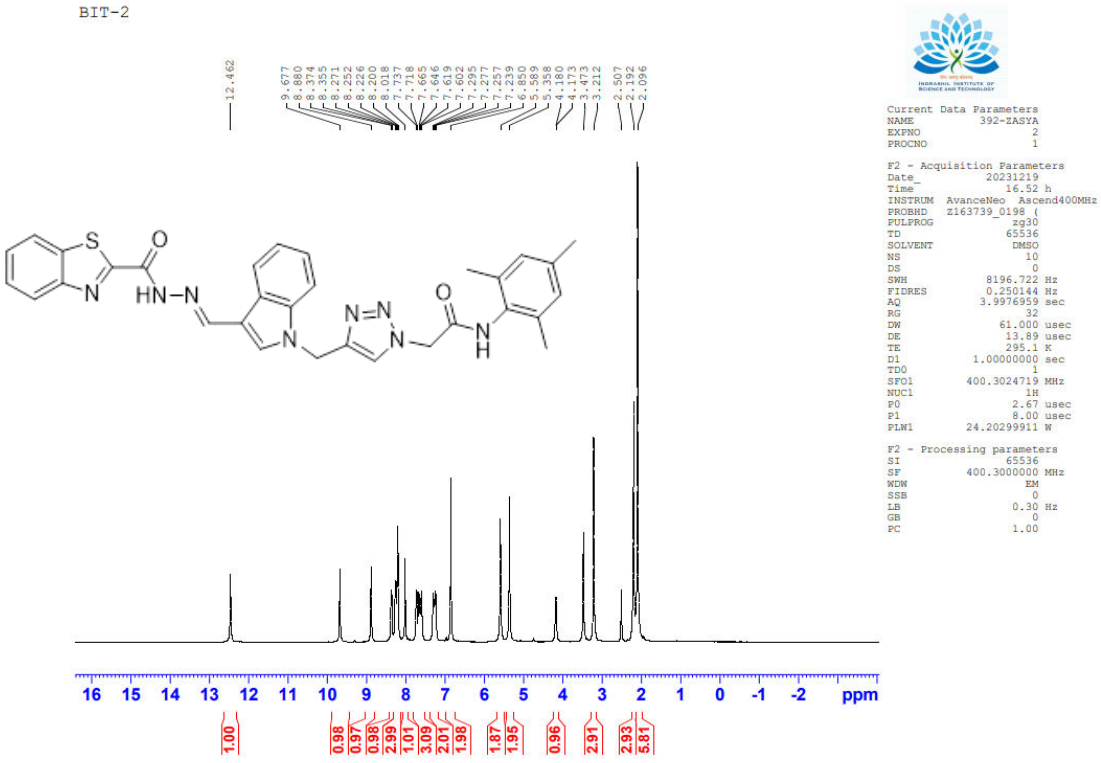

Figure 10: Representative ^{1}H NMR spectrum of compound 8b

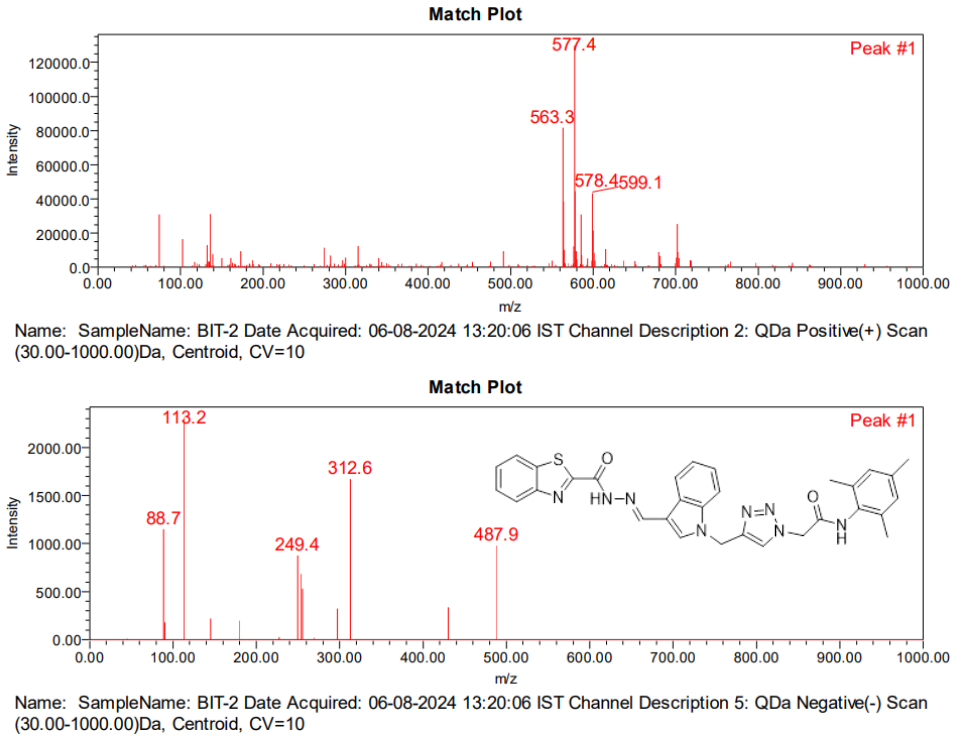

Figure 11: Representative mass spectrum of compound 8b

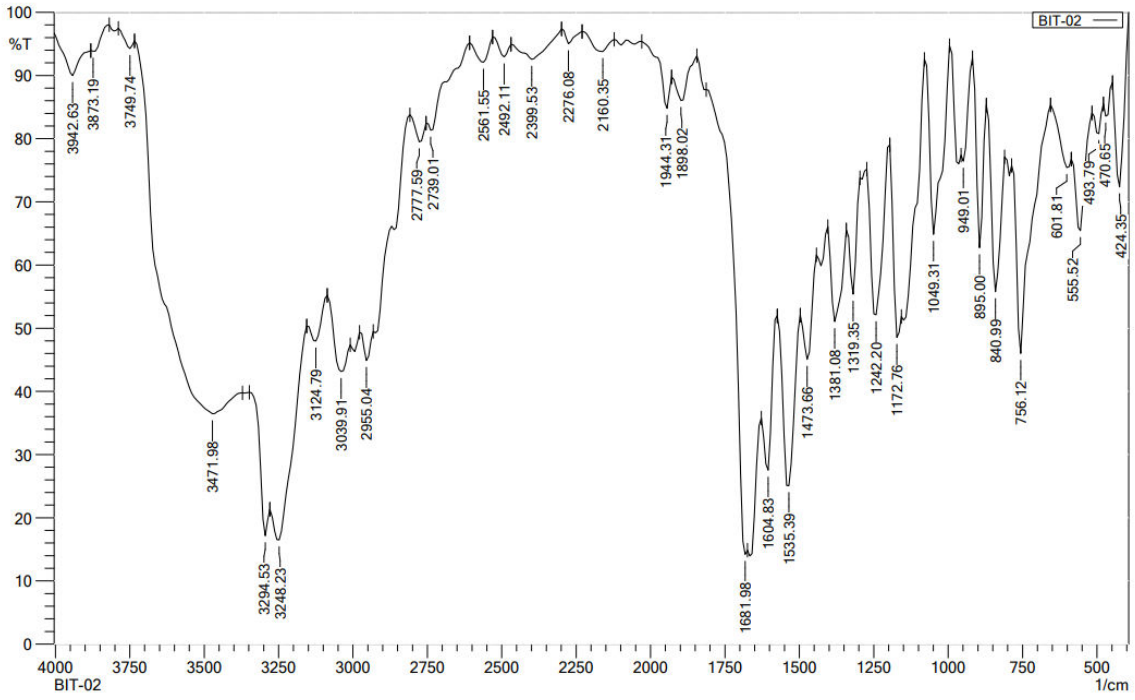

Figure 12: Representative FT-IR spectrum of compound 8b

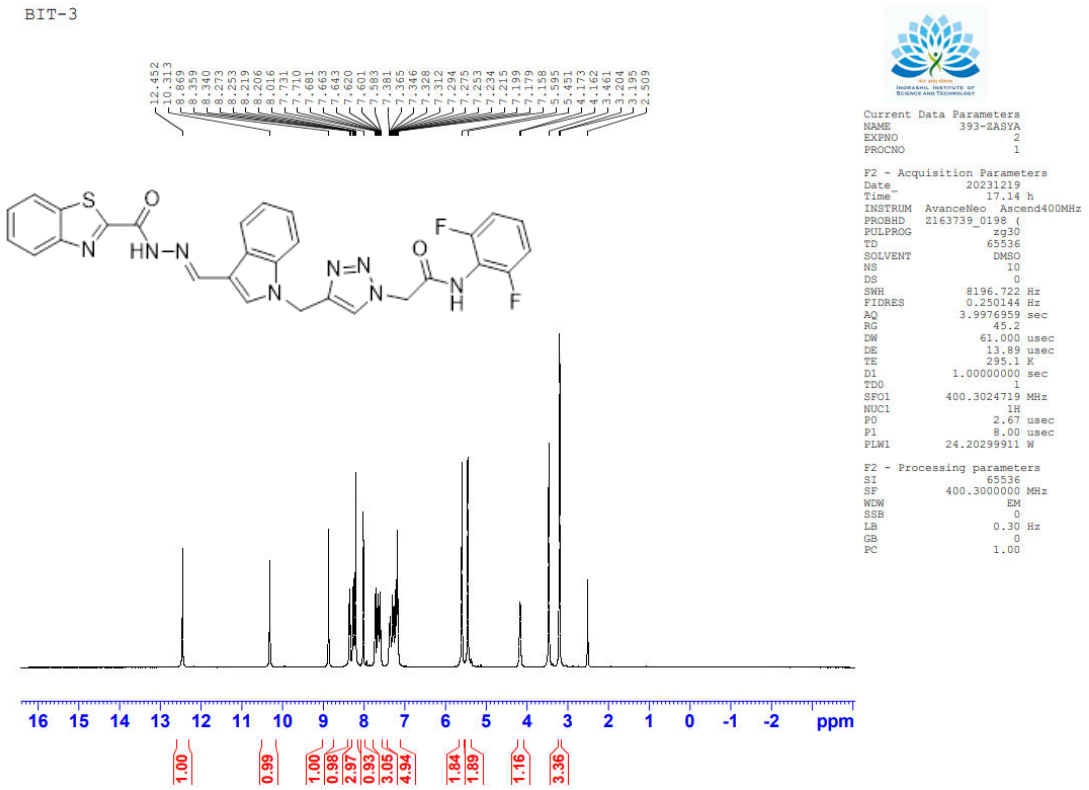

Figure 13: Representative ^{1}H NMR spectrum of compound 8c

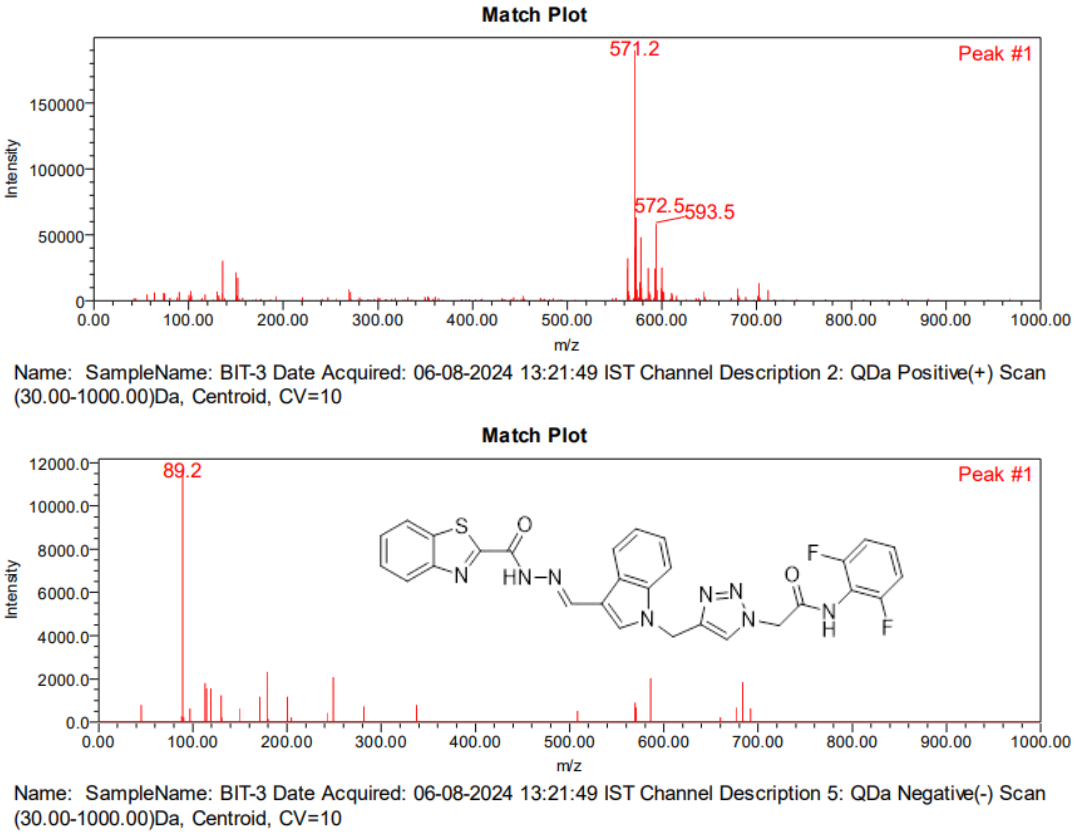

Figure 14: Representative mass spectrum of compound 8c

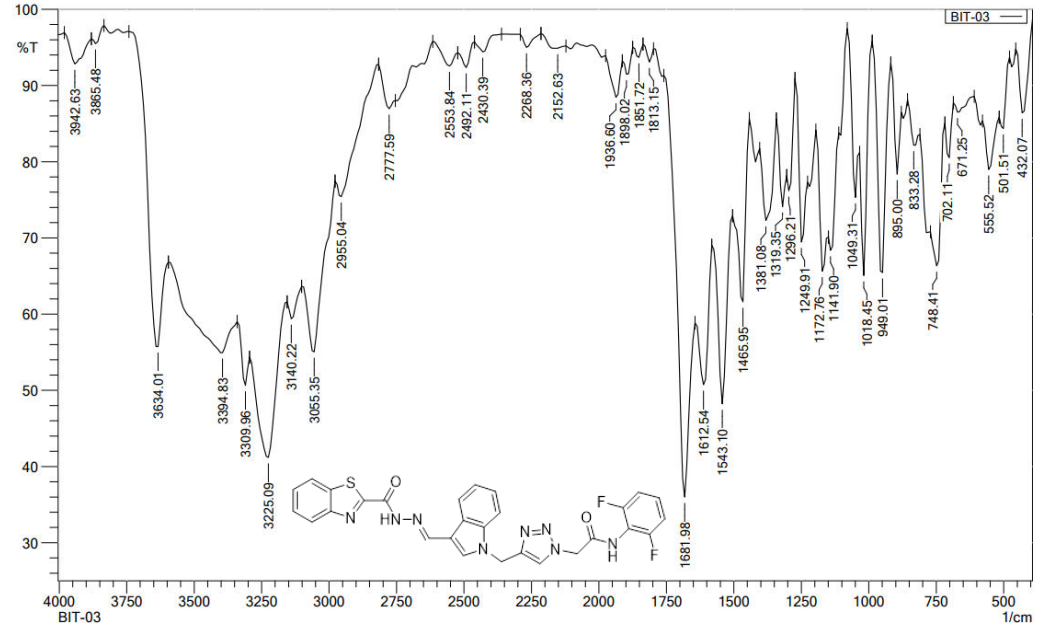

Figure 15: Representative FT-IR spectrum of compound 8c

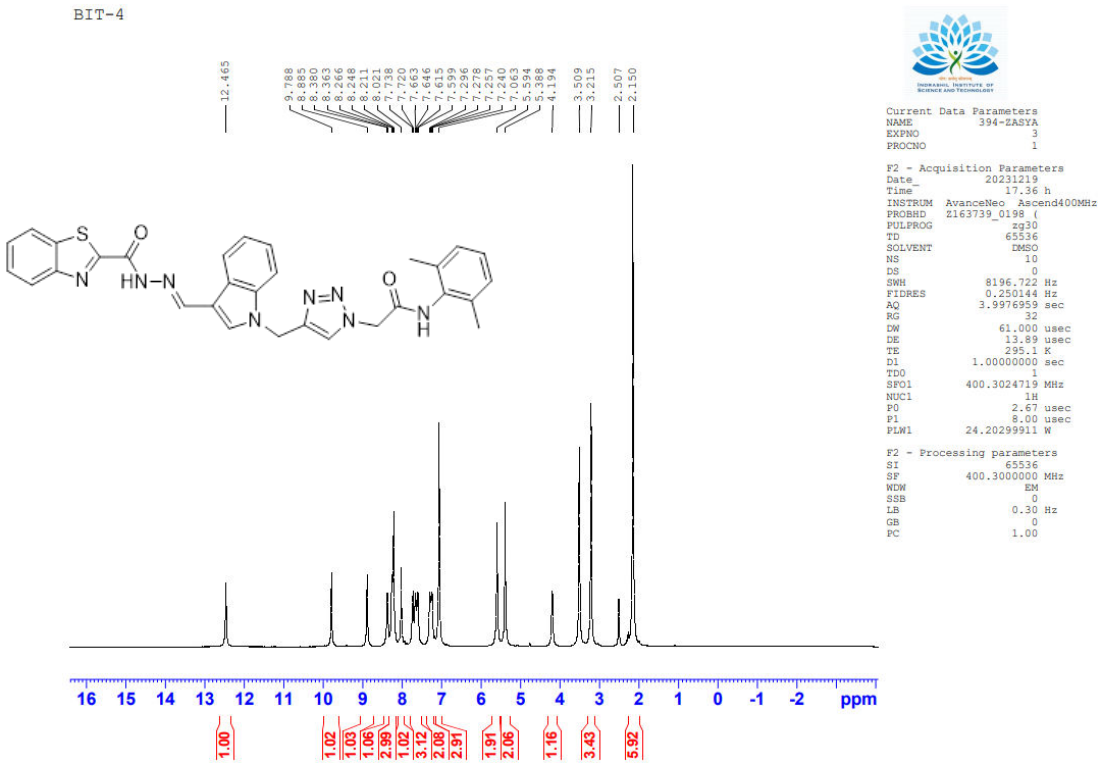

Figure 16: Representative ^{1}H NMR spectrum of compound 8d

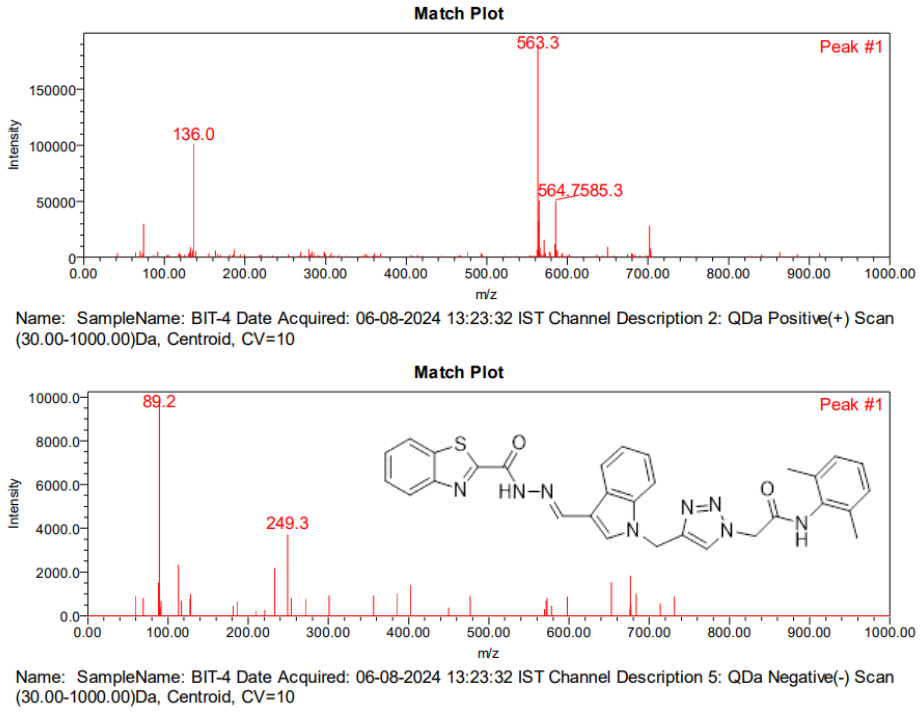

Figure 17: Representative mass spectrum of compound 8d

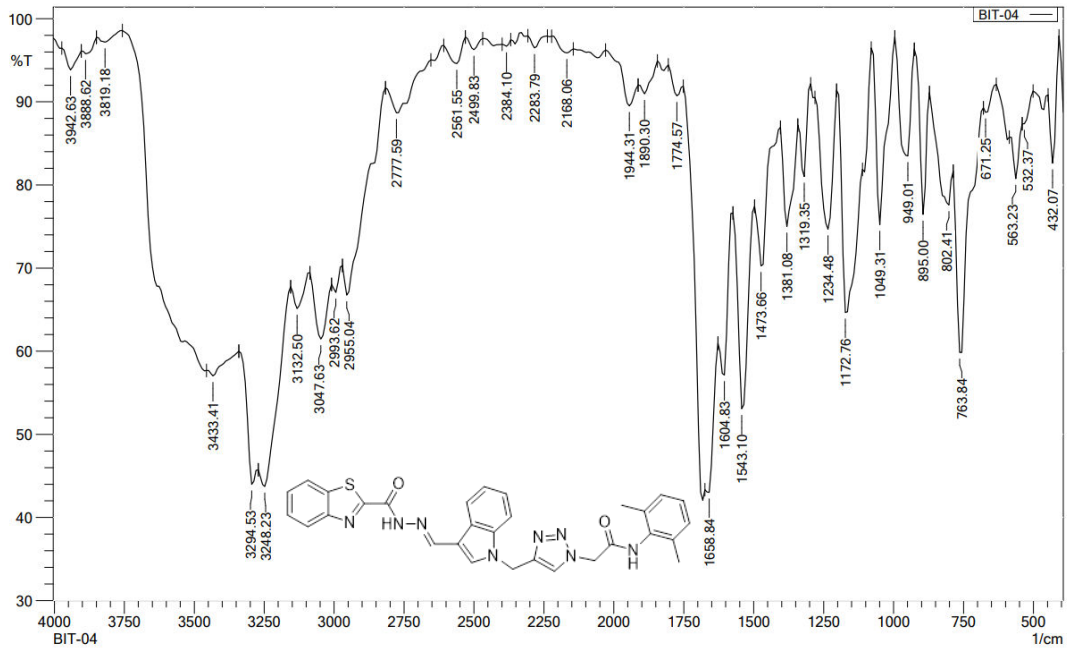

Figure 18: Representative FT-IR spectrum of compound 8d

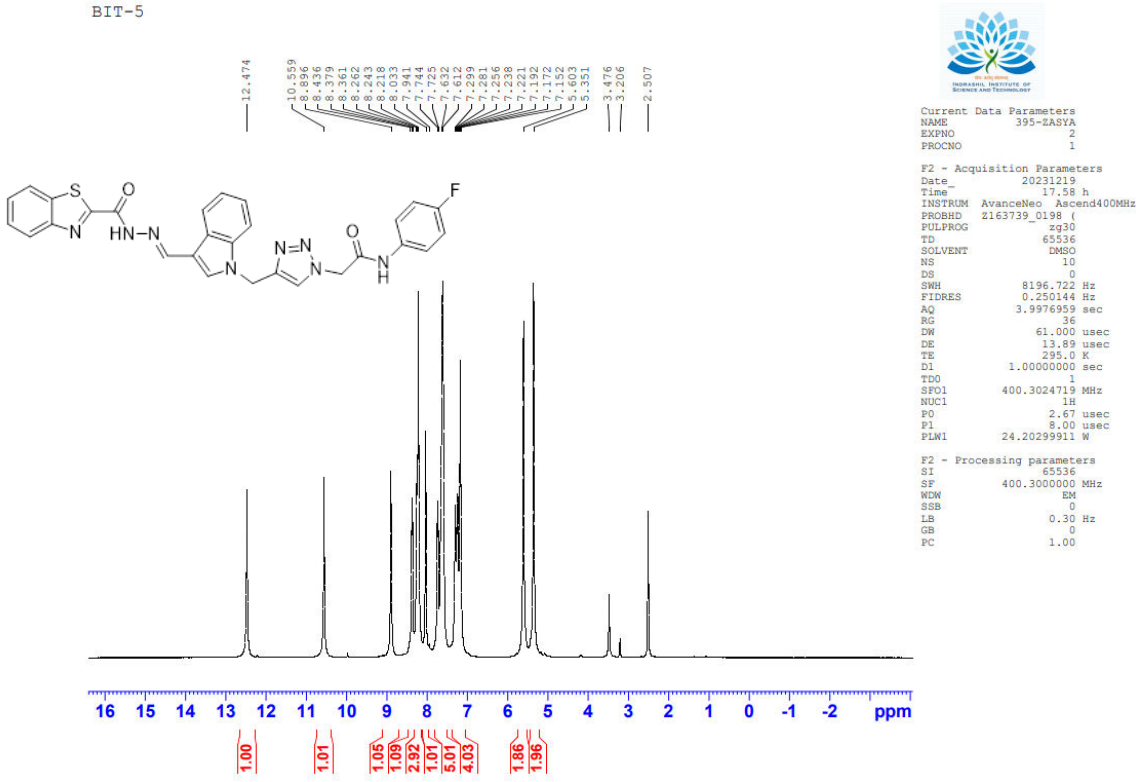

Figure 19: Representative ^{1}H NMR spectrum of compound 8e

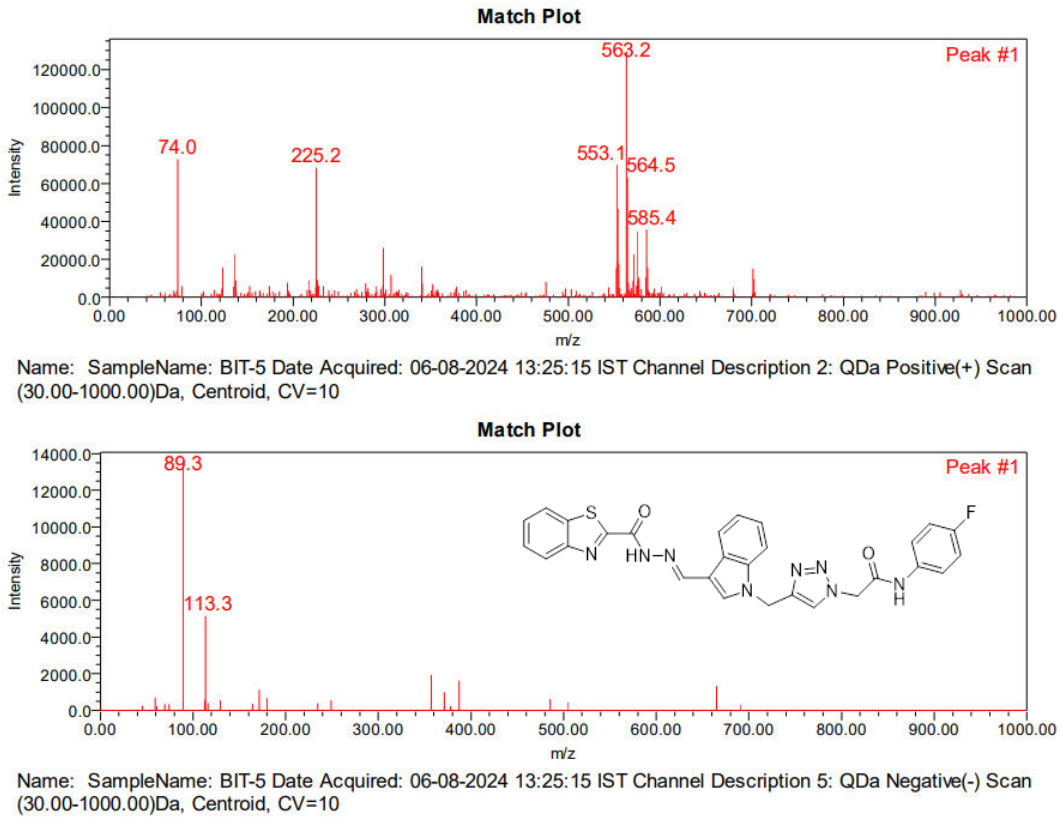

Figure 20: Representative mass spectrum of compound 8e

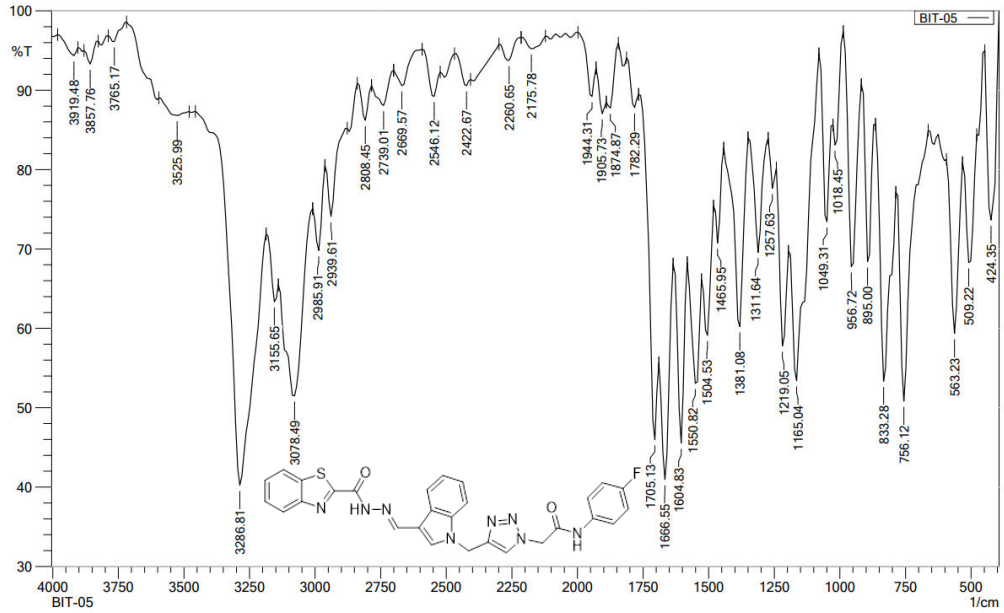

Figure 21: Representative FT-IR spectrum of compound 8e

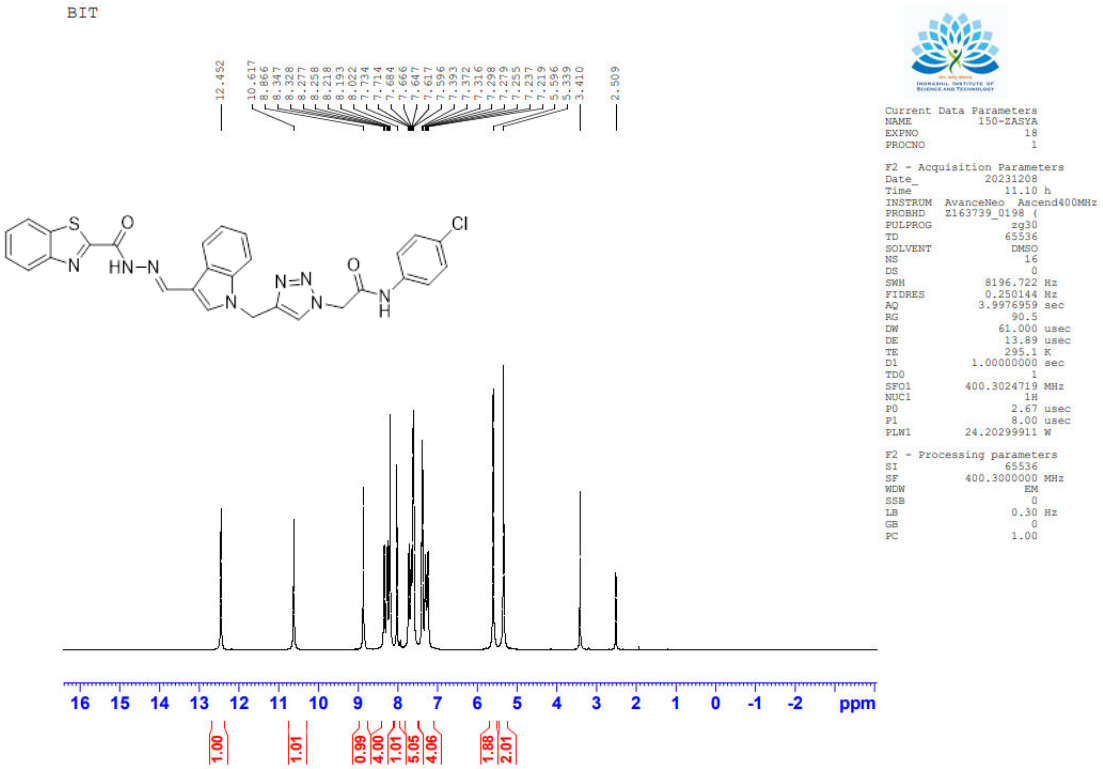

Figure 22: Representative ^{1}H NMR spectrum of compound 8f

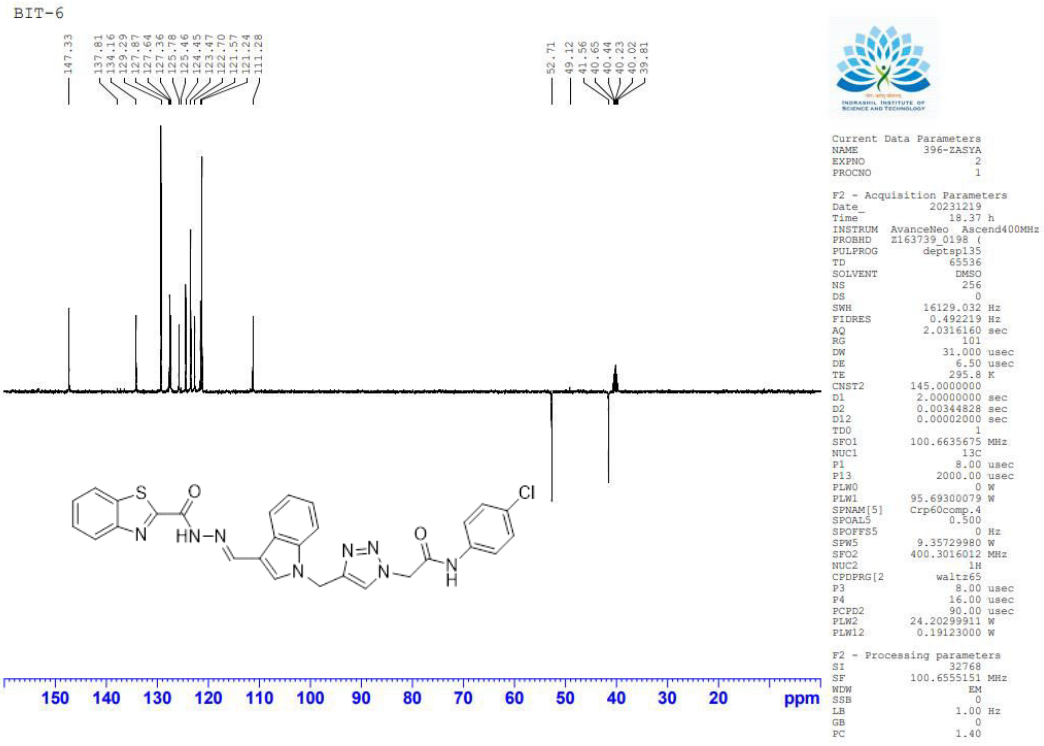

Figure 23: Representative ^{13}C NMR spectrum of compound 8f

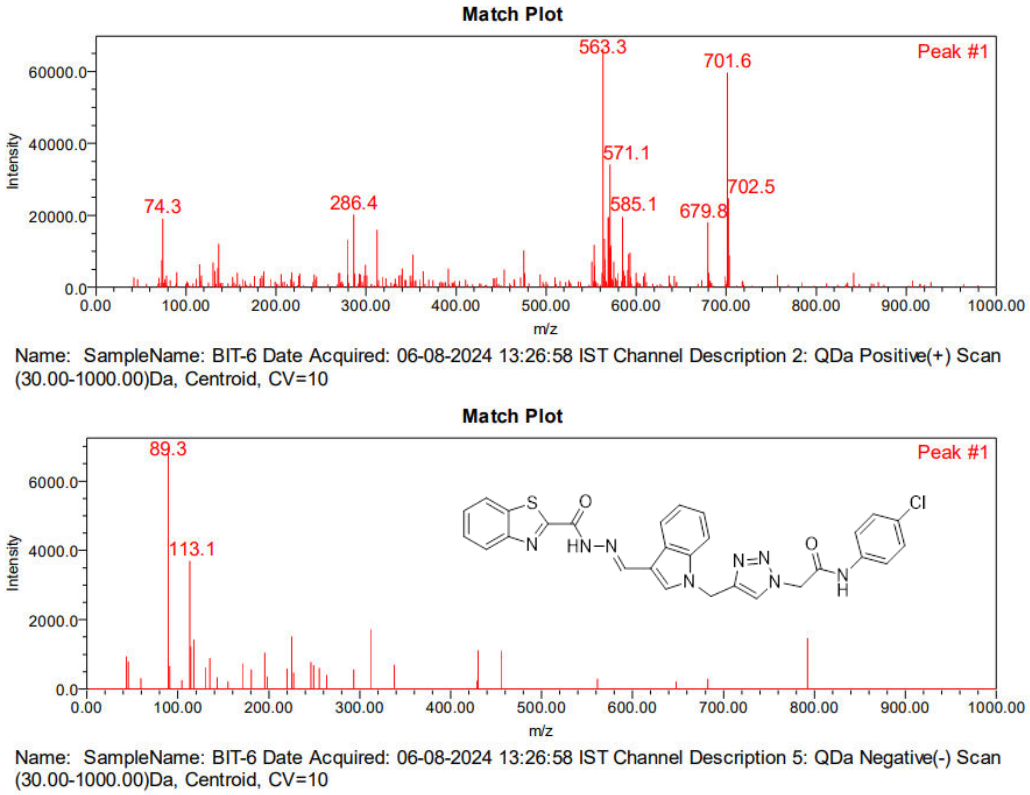

Figure 24: Representative mass spectrum of compound 8f

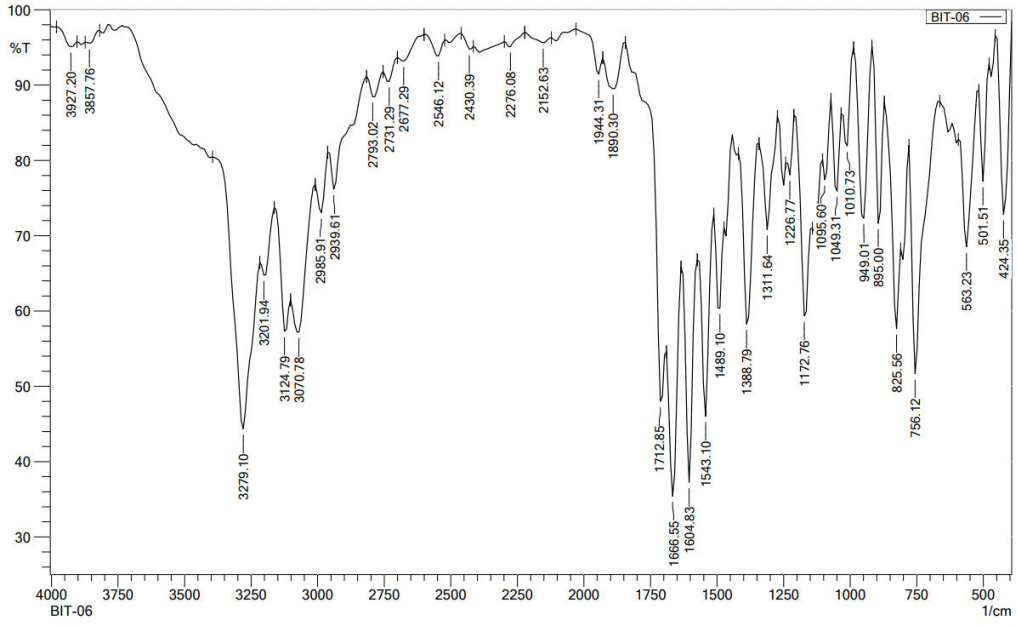

Figure 25: Representative FT-IR spectrum of compound 8f

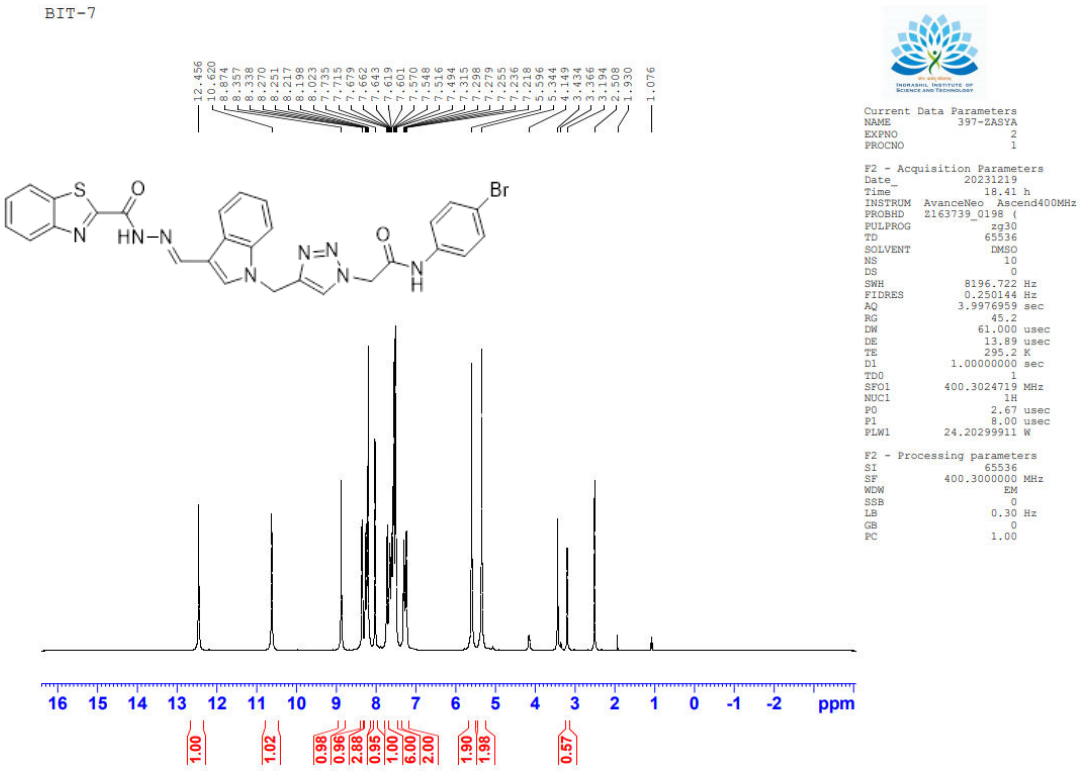

Figure 26: Representative ^{1}H NMR spectrum of compound 8g

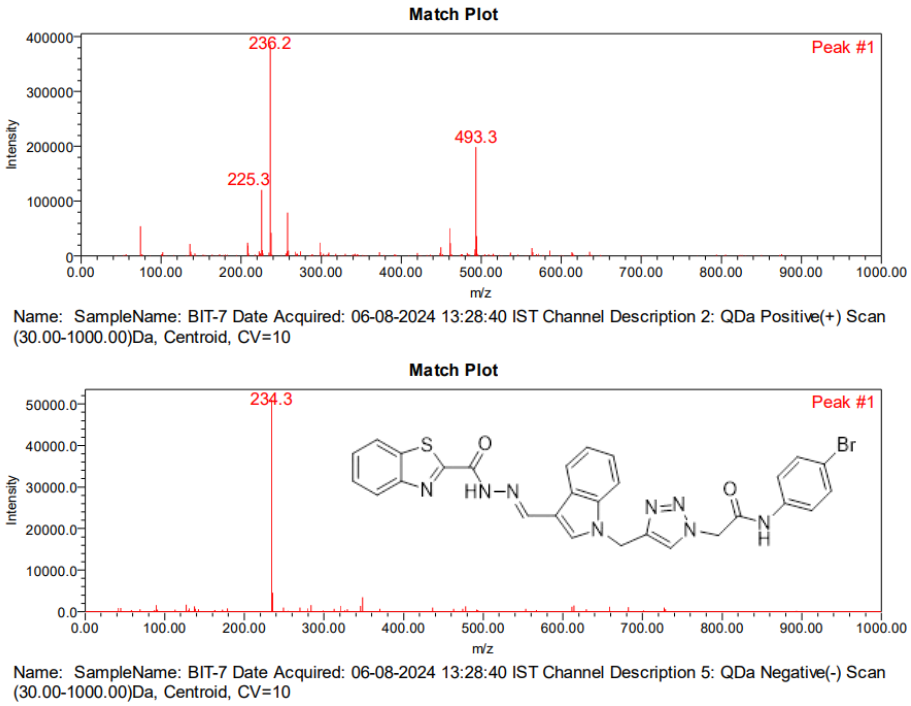

Figure 27: Representative mass spectrum of compound 8g

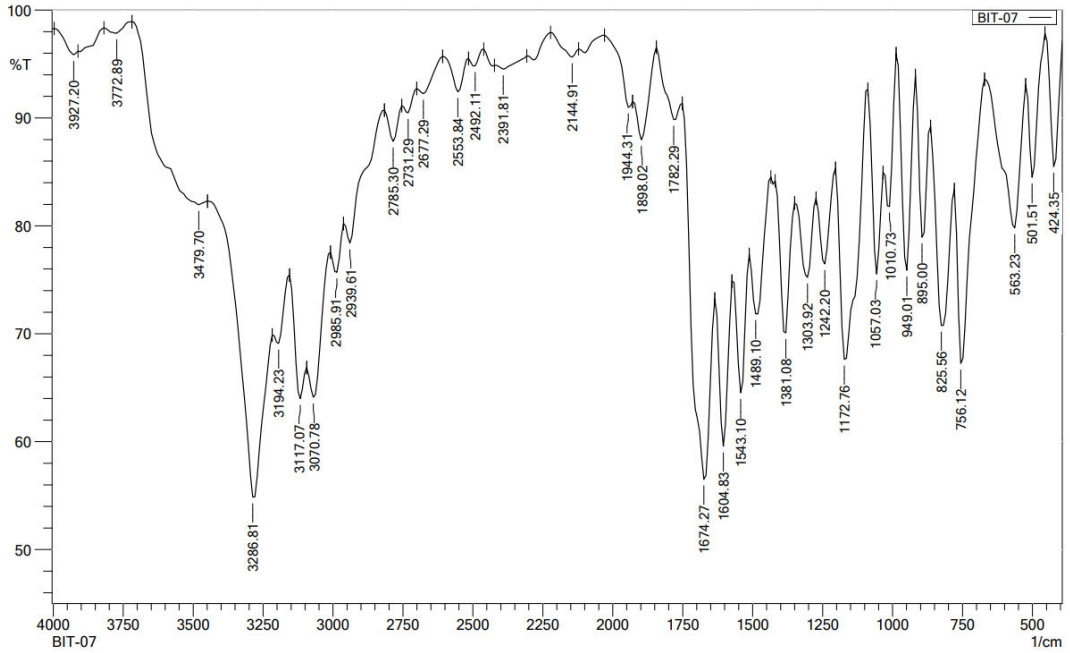

Figure 28: Representative FT-IR spectrum of compound 8g

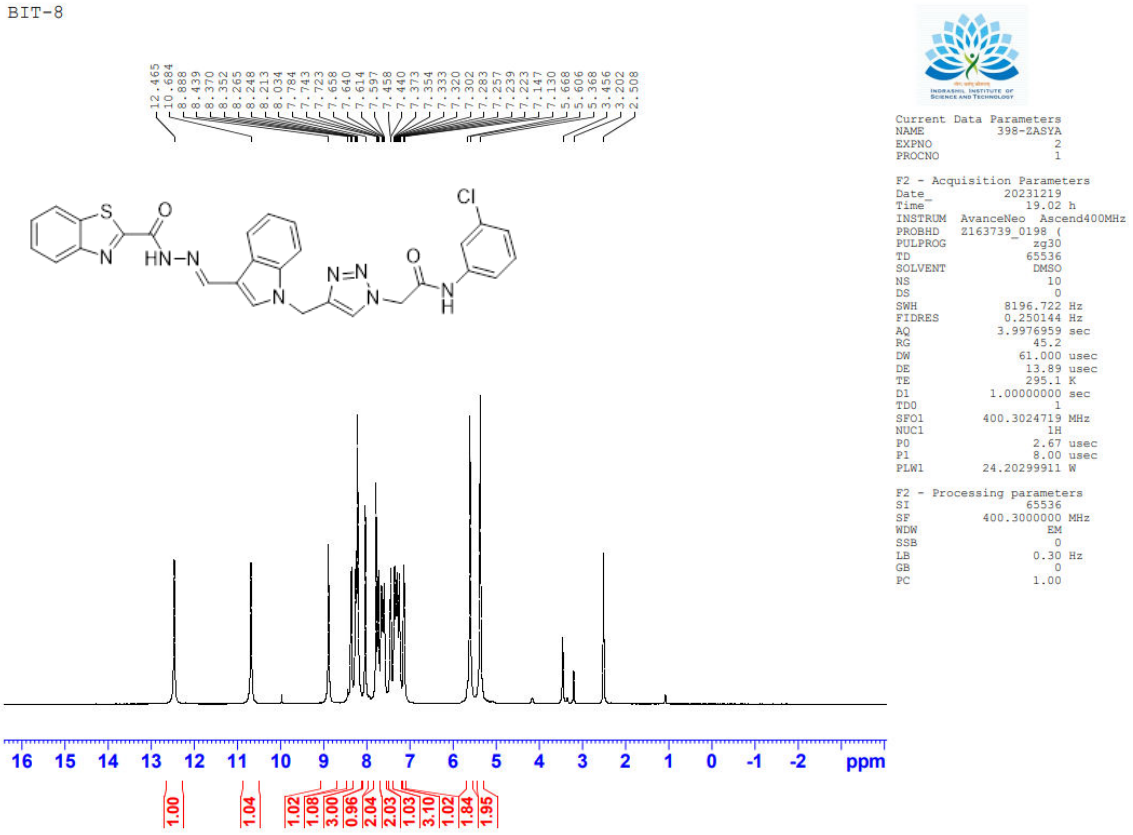

Figure 29: Representative ^{1}H NMR spectrum of compound 8h

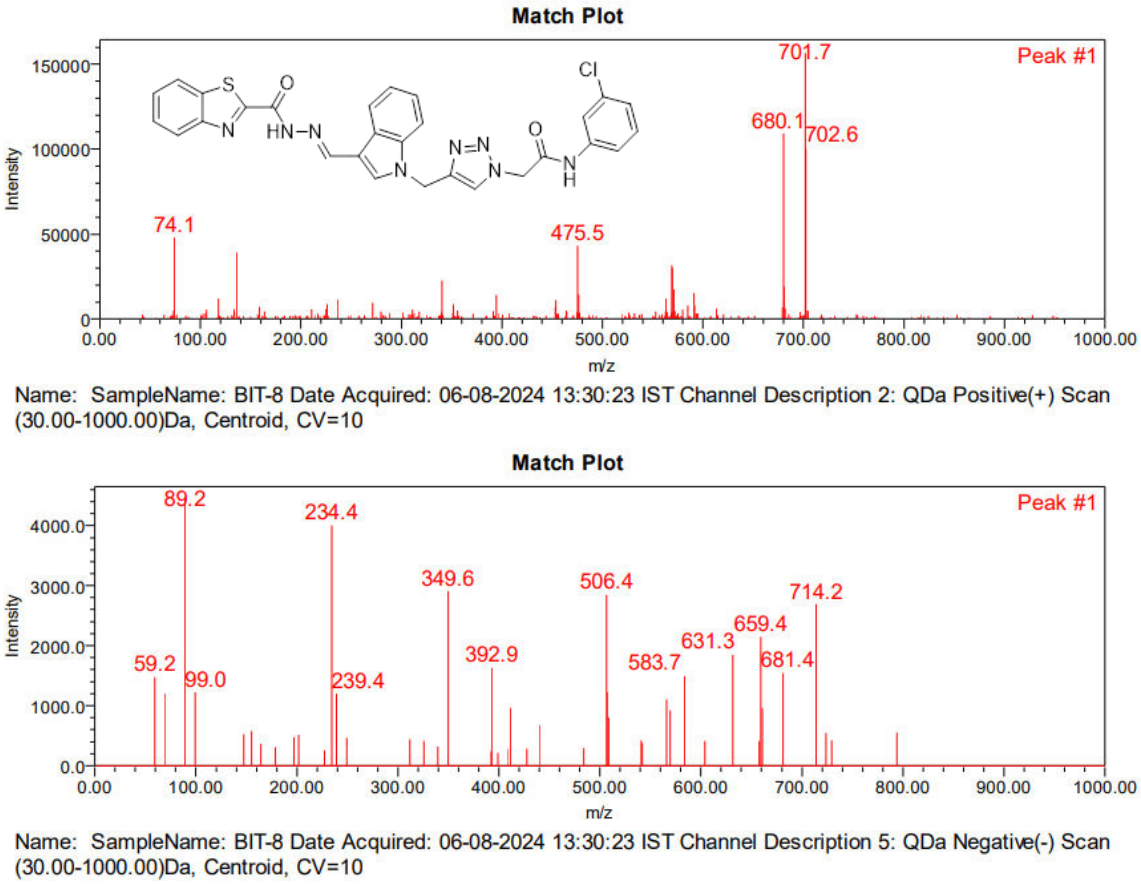

Figure 30: Representative mass spectrum of compound 8h

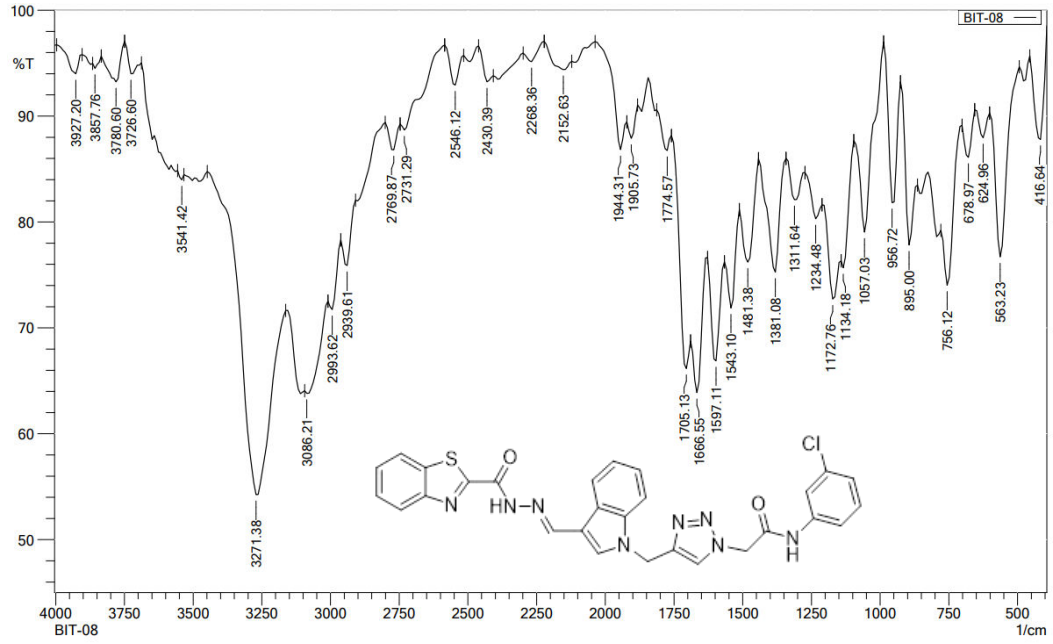

Figure 31: Representative FT-IR spectrum of compound 8h

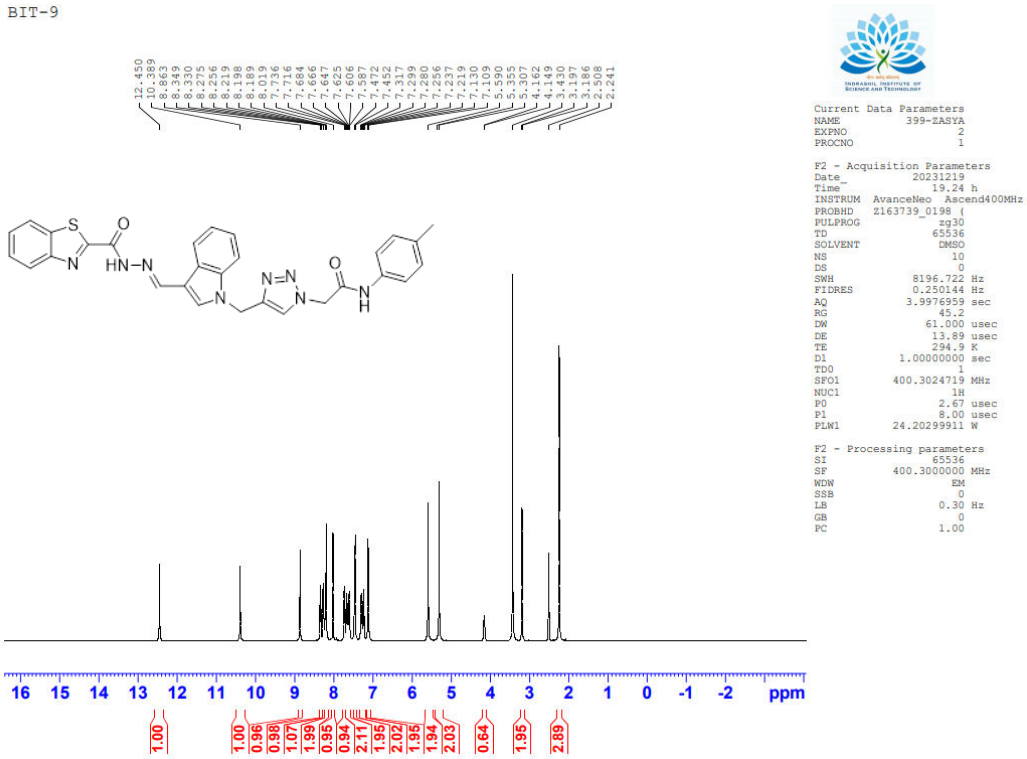

Figure 32: Representative ^{1}H NMR spectrum of compound 8i

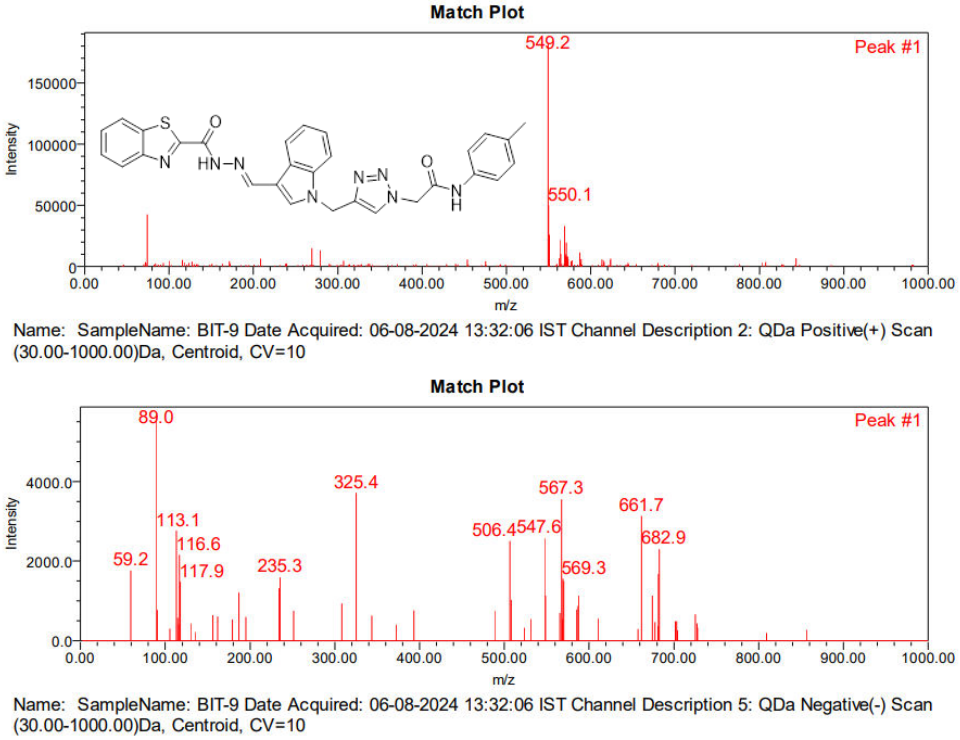

Figure 33: Representative mass spectrum of compound 8i

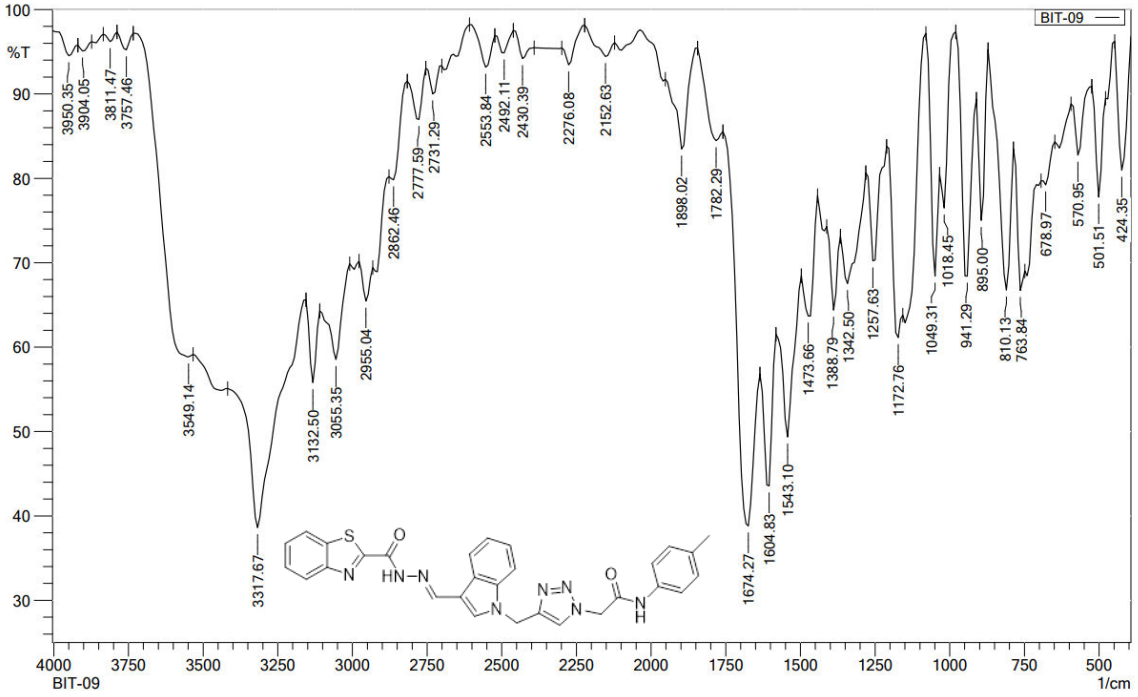

Figure 34: Representative FT-IR spectrum of compound 8i

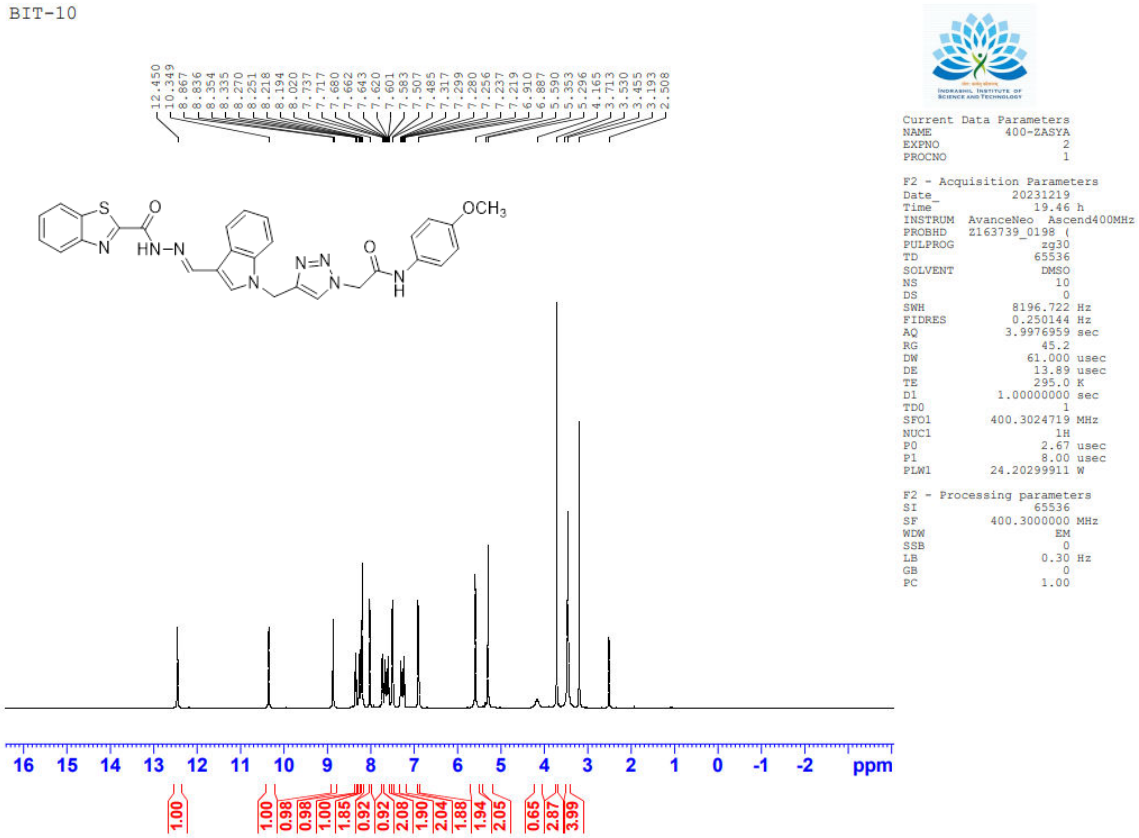

Figure 35: Representative ^{1}H NMR spectrum of compound 8j

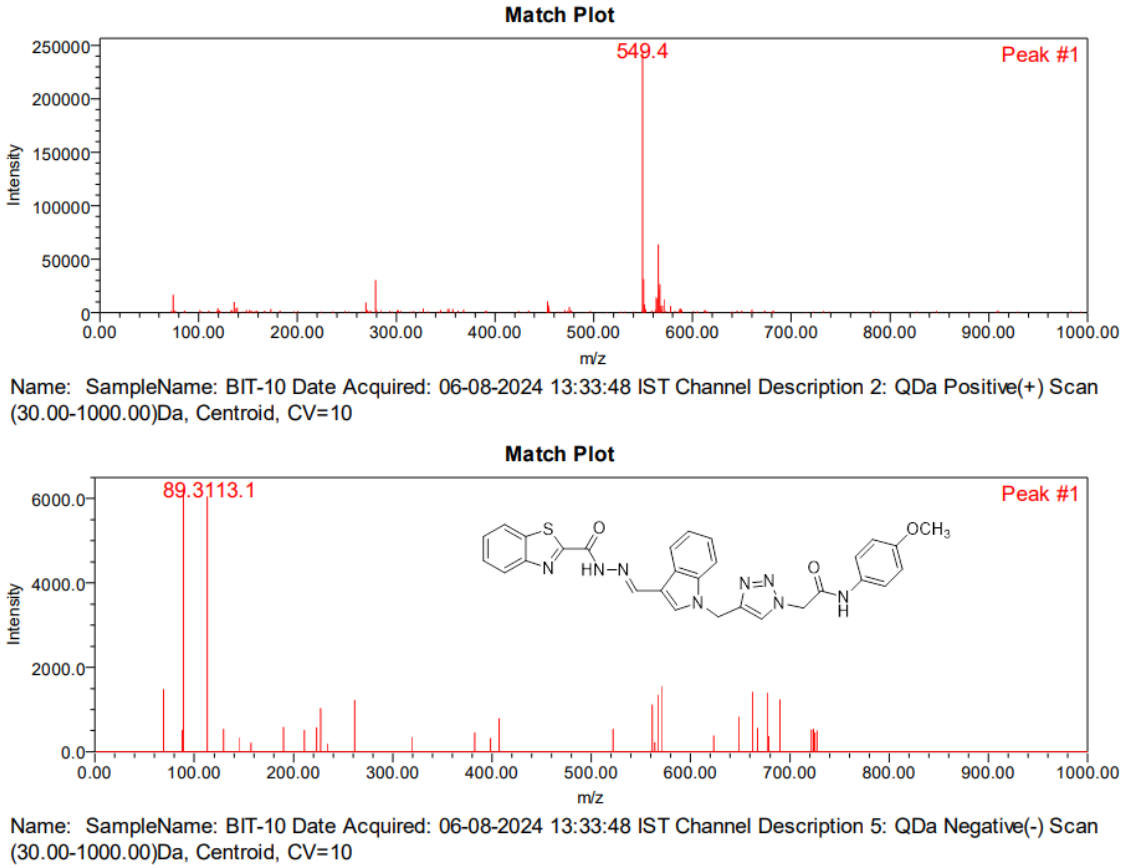

Figure 36: Representative mass spectrum of compound 8j

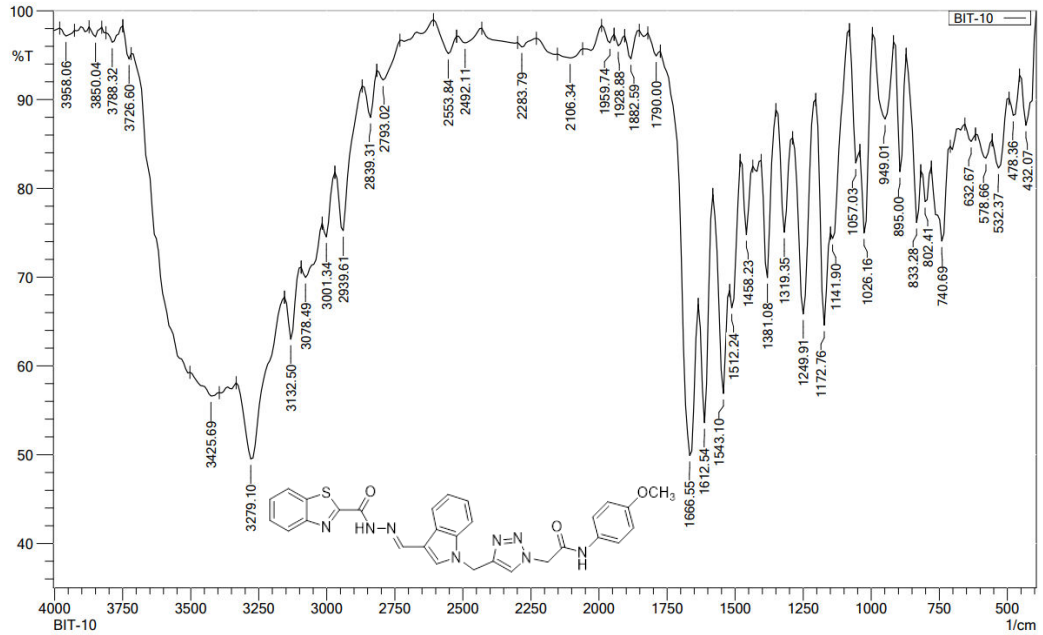

Figure 37: Representative FT-IR spectrum of compound 8j